

**SPATIAL ANALYSIS OF POSITRON EMISSION TOMOGRAPHY IMAGES OF
PARKINSON'S DISEASE USING 3D MOMENT INVARIANTS**

by

MARJORIE EMILY GONZALEZ

A THESIS SUBMITTED IN PARTIAL FULFILLMENT OF
THE REQUIREMENTS FOR THE DEGREE OF
MASTER OF SCIENCE

in

THE FACULTY OF GRADUATE STUDIES

(Physics)

THE UNIVERSITY OF BRITISH COLUMBIA

(Vancouver)

August 2012

© Marjorie Emily Gonzalez, 2012

Abstract

Positron emission tomography (PET) produces images of functional processes of the body *in-vivo*. The analysis of PET data for research purposes traditionally involves kinetic modeling of the concentration of the radiotracer over time within a region of interest (ROI) in the body to derive parameters related to the uptake/binding of the radiotracer in that region. PET imaging is commonly used to study Parkinson's disease (PD), where loss of motor function is caused by the progressive death of neurons in the brain that produce the neurotransmitter dopamine. In PD, both the kinetic and the spatial distribution of the tracer change due to the disease: the posterior parts of the striatum (in particular in the putamen) are affected before the anterior parts.

The purpose of this dissertation is to develop a novel analysis method for PET data that uses the spatial characteristics of the radiotracer's distribution within anatomically-defined ROIs to extract additional information about pathological states. The proposed analysis method is based on mathematical 3D shape descriptors that are invariant to translation, scaling, and rotation, called 3D moment invariants (3DMIs). The variable of interest in this case is not only the radiotracer's uptake rate constant or binding potential, but also the 3D spatial shape and distribution of the radioactivity within the ROI.

This dissertation shows that 3DMIs were able to successfully quantify differences in the spatial distribution of PET radiotracer images between healthy controls and PD subjects. 3DMI values were found to correlate with a clinical measure of disease severity in all anatomical regions studied here (putamen, caudate and ventral striatum), as opposed to kinetic parameters which only showed significant correlation to clinically-assessed PD severity in the putamen. Levodopa-induced changes in spatial patterns of dopamine release (as measured using 3DMIs) were found to be significantly correlated with PD severity in all ROIs studied here. These findings suggest that quantitative studies of a radiotracer's spatial distribution can be complementary to kinetic modeling in extracting information about pathological states from PET data and have the potential to contribute novel information in PET neuroimaging studies.

Preface

Versions of Chapter 4 and Chapter 5 have been submitted for publication as Gonzalez, M. E., Dinelle, K., Vafai, N., Heffernan, N., MacKenzie, J., Cresswell, S., McKeown, M., Stoessl, A. J., Sossi, V. (2012) *Novel Spatial Analysis Method for PET Images using 3D Moment Invariants: Applications to Parkinson's disease*. I conducted all the data taking, processing, analysis and wrote the entire manuscript.

The data used here was collected as part of the study called “Studies of Treatment-Related Compulsive Behaviors and Impulse Control Disorders in Parkinson's Disease”. This study received approval from the UBC Clinical Research Ethics Board for studies involving human subjects. The certificate number is H08-00770.

Table of Contents

Abstract	ii
Preface	iii
Table of Contents	iv
List of Tables	vii
List of Figures	viii
Glossary	xi
Acknowledgements	xiii
Dedication	xiv
Chapter 1: Introduction	1
1.1 PET Basics.....	1
1.2 PET Instrumentation.....	2
1.3 Data Acquisition.....	5
1.4 Data Corrections.....	8
1.5 Image Reconstruction.....	10
1.6 Data Analysis: Kinetic Modeling.....	12
1.7 MRI Basics.....	16
1.8 Thesis Motivation and Outline.....	18
Chapter 2: Moment Invariants	21
2.1 Introduction.....	21

2.2	2D Moments.....	22
2.2.1	Invariance to Translation	23
2.2.2	Invariance to Scaling	24
2.2.3	Invariance to Rotation.....	25
2.3	3D Moment Invariants	26
2.4	Applications in Medical Imaging.....	28
2.5	3D Moment Invariants for PET Images	29
Chapter 3: Parkinson’s Disease		30
3.1	Clinical Overview	30
3.2	Neuroanatomy of Motor Function	33
3.3	Dopamine System	36
3.4	PET Imaging of PD.....	38
Chapter 4: 3D Moment Invariants for PET Images of Parkinson’s Disease		42
4.1	Introduction.....	42
4.2	Materials	43
4.2.1	PET Data.....	43
4.2.2	MRI Data	44
4.2.3	Subject Details	44
4.3	Methodology	45
4.3.1	Data Analysis.....	45
4.3.2	3DMIs for PET Data.....	48

4.4	Results.....	49
4.4.1	3DMIs Differentiate Between Healthy Controls and PD patients	49
4.4.2	3DMIs Correlate with PD Severity.....	54
4.4.3	Levodopa-induced Spatial Changes Correlate with PD Severity	58
Chapter 5: Discussion, Future Work and Conclusions.....		63
5.1	Discussion and Future Work.....	63
5.2	Conclusions.....	65
Bibliography.....		67

List of Tables

Table 4.1: <i>Subject demographics</i> *	45
Table 4.2: <i>Statistical differences (p- values) between healthy controls and PD subjects.</i>	52
Table 4.3: <i>Regression parameters for 3DMIs as a function of UPDRS for PD subjects. An exponential relationship was assumed and subsequently linearized.</i>	57

List of Figures

Figure 1.1: <i>Sample configuration for PET detectors using a ring (A) and hexagonal (B) geometry. Scintillation crystals can be designed in small elements (A) or larger continuous elements (B).</i>	3
Figure 1.2: <i>A) Schematic of PET detectors consisting of scintillation crystals and PMTs. B) Block detector configuration with many crystal elements (separated by lightguides) sharing a few PMTs.</i> ...	4
Figure 1.3: <i>Schematic showing the LOR parameters ($\mathbf{r}, \theta, \varphi, \mathbf{z}$) from a transaxial (left) and axial (right) view.</i>	6
Figure 1.4: <i>Left – sample projections of a point source at two different transaxial angles. Right – Corresponding sinogram.</i>	7
Figure 1.5: <i>Sample schematic showing true (left), scattered (center) and random (right) coincidences detected by PET systems.</i>	8
Figure 1.6: <i>Schematic summary of the key steps in iterative reconstruction.</i>	12
Figure 1.7: <i>Simple two-compartment kinetic model with rate constants k_1 and k_2 and concentrations in each compartment of $C_A(t)$ and $C_B(t)$.</i>	13
Figure 1.8: <i>Sample TACs for the putamen (tissue of interest) and the cerebellum (reference tissue) using the radiotracer [^{11}C]Raclopride.</i>	14
Figure 1.9: <i>Kinetic model using a reference region as the input function.</i>	15
Figure 1.10: <i>A – Schematic showing alignment of nuclear magnetic moments in the presence of an external magnetic field (B_0). B – Use of an RF pulse to flip spins and their subsequent relaxation.</i> ...	16
Figure 1.11: <i>Sample T1-weighted MR image.</i>	17
Figure 2.1: <i>Sample distributions showing the shape characteristics that can be described using moments.</i>	24
Figure 3.1: <i>Anatomy of the basal ganglia in sagittal (left) and transverse planes (right).</i>	33

Figure 3.2: <i>The classical basal ganglia circuits involved in motor (A) and limbic (B) functions.</i>	34
Figure 3.3: <i>Schematic of a dopaminergic synapse showing pre-synaptic and post-synaptic components.</i>	37
Figure 3.4: <i>PET images using RAC (left), DTBZ (middle) and FDOPA (right) for a healthy control (top) and a subject with PD (bottom).The more affected side for this PD subject is the left side.</i>	39
Figure 4.1: <i>Left - DTBZ images over three brain slices for a healthy control (top) and PD patient (bottom) with corresponding ROIs for the caudate and putamen. Right - Sample spatial distributions extracted for the right putamen for both subjects.</i>	47
Figure 4.2: <i>Left - Spatial variance (J_1) for healthy controls and PD subjects in the putamen, caudate and ventral striatum obtained from DTBZ (dot), FDOPA (square) and RAC (cross) images. Individual error bars in J_1 values were found by bootstrapping. Right - DTBZ BP, FDOPA Kocc and RAC BP values for the same ROIs.</i>	51
Figure 4.3: <i>Spatial asymmetry (as measured using B_3) for healthy controls and PD subjects in the putamen for DTBZ (dots), FDOPA (square) and RAC (cross)</i>	52
Figure 4.4: <i>Spatial variance (J_1, top) and asymmetry (B_3, bottom) for all ROIs with voxel values replaced by 1.</i>	54
Figure 4.5: <i>Spatial variance (J_1) in DTBZ images as a function of UPDRS (left) and DTBZ BP (middle) for the putamen (top), caudate (center) and ventral striatum (bottom). The corresponding values for DTBZ BP versus UPDRS are also shown (right). Each side of the brain is shown separately.</i>	56
Figure 4.6: <i>Spatial asymmetry (B_3) in DTBZ images of the putamen as a function of UPDRS (left) and DTBZ BP (right).</i>	57
Figure 4.7: <i>Levodopa-induced changes in the putamen. Left: RAC J_1 (top) and BP_{ND} (bottom) values for healthy controls, PD patients at baseline and PD after LD. Middle: Levodopa-induced changes in RAC J_1 (top) and DA release (bottom) as a function of UPDRS.Right: Levodopa-induced change in RAC J_1 (top) and DA release (bottom) as function of DTBZ BP.</i>	59
Figure 4.8: <i>Same as Figure 4.7 but for the caudate.</i>	61

Figure 4.9: *Same as Figure 4.7 but for the ventral striatum.* 62

Glossary

3DMIs	3D moment invariants
BP	Binding potential
DA	Dopamine
DTBZ	[¹¹ C]Dihydrotetrabenazine
FBP	Filtered backprojection
FDOPA	[¹⁸ F]Fluoro-L-dopa
FDG	[¹⁸ F]Fluorodeoxyglucose
FOV	Field of view
GPe	External globus pallidus
GPi	Internal globus pallidus
H&Y	Hoehn & Yahr scale
K_{occ}	FDOPA uptake rate constant
LD	Levodopa
LOR	Line of response
MRI	Magnetic resonance imaging
OSEM	Ordered subset expectation maximization
PET	Positron emission tomography
PD	Parkinson's disease
PMT	Photo-multiplier tube
RAC	[¹¹ C]Raclopride
RF	Radio frequency
ROI	Region of interest

SNe	Substantia nigra pars compacta
SNr	Substantia nigra pars reticulata
STN	Subthalamic nucleus
TAC	Time activity curve
TE	Echo time
TR	Repetition time
UPDRS	United Parkinson's disease rating scale
VMAT2	Vesicular monoamine transporter type 2
VS	Ventral striatum
VTA	Ventral tegmental area

Acknowledgements

I would like to give many thanks to my supervisor, Vesna Sossi, for her help and support during my degree. Her dedication and enthusiasm for the field are incredibly inspiring and she made this great learning experience much more enjoyable. It has also been a pleasure to work with the rest of the UBC PET group: Katie Dinelle, Nasim Vafai, Matt Walker, Stephan Blinder, Siobhan McCormick, Geoff Topping, Ivan Klyuzhin, Greg Stortz, Ryan Thompson and Carolyn English. Thank you to everyone at TRIUMF for their help and dedication to every tracer delivery. A lot of thanks are also due to those of you at the Pacific Parkinson's Research Centre who are on the front lines of patients' lives and remind us why we do what we do: Jess McKenzie, Nicole Heffernan, Martin McKeown, Jon Stoessl and Silke Appel-Cresswell. You all have contributed to this work and I have learned a great deal from all of you. Thank you.

Finally, a special thanks to all my family for their love and support. I would not have been able to do this without you. To my parents, thank you for being there for me no matter what and for making me who I am. To my brothers, thank you for being the best brothers and friends I could ask for. To Lateef, thank you for putting it up with me, for supporting me, for accompanying me in this journey and for making my life better everyday.

Dedication

Para Mama Mila,

siempre la llevamos con nosotros, en todo lo que hacemos y todo lo que somos.

Chapter 1: Introduction

1.1 PET Basics

Medical imaging aims to produce images of selected characteristics of the human body to help with patient care and medical research. Positron emission tomography (PET) is a medical imaging modality that allows us to produce images of functional processes of the body *in-vivo* (Bailey, 2005). An image is produced by detecting pairs of γ -rays emitted indirectly from a molecule that tracks a specific body function. In order to emit γ -rays, the molecule is first tagged in a radiochemistry laboratory with a positron-emitting isotope which decays by the conversion of a proton into a neutron and producing a positron and neutrino as by-products:



The radiolabeled molecule is then introduced in the body, where the positron travels until it encounters an electron (β). The $\beta\beta^+$ pair annihilates and two nearly collinear γ -rays are emitted, each with an energy of 511 keV. These γ -rays can be detected with specialized instruments and used to produce an image of where the molecule is located.

The molecules used for PET imaging have to reflect a specific function in the body. For example, the molecule fluorodeoxyglucose (FDG) can be labeled with β^+ -emitting ^{18}F and used as an analogue of glucose. Glucose is widely used by cells in the body as a main source of energy and ^{18}F -FDG can be used to image a wide range of clinical conditions, such as rapidly-growing tumors (Chen and Chen, 2011).

Other commonly used β^+ -emitting isotopes for PET imaging are ^{11}C , ^{15}O , ^{13}N and ^{82}Rb . The presence of a neutrino in the decay (see Equation 1.1) allows some of the energy and momentum of the original proton to be carried away. Therefore, emitted positrons can have a continuum of kinetic energies up to a maximum value, which depends on the nuclear states of the parent and daughter isotopes. The positron can then travel a wide range of distances in

the body before it loses all its kinetic energy and annihilates with an electron. For example, the mean(maximum) positron range in water for ^{18}F , ^{11}C and ^{15}O is 0.6(2.4) mm, 1.1(4.1) mm and 2.5(7.3) mm, respectively (Bailey, 2005). Isotopes with low positron range are ideal for PET imaging because they allow for a better localization of the radiolabeled molecule within the body.

Radioactive decay follows an exponential form, with the number of decays being proportional to the amount of material available to decay ($N = N_0 e^{-\lambda t}$, where N_0 is the original number of decaying isotopes). The rate at which the decay takes place (called *radioactivity*¹) is described by the decay constant, λ . An intuitive way to characterize the decay is by determining the time it takes for half the material to decay, also called the half-life, given by $T_{1/2} = \ln 2/\lambda$. For example, the half-life of ^{18}F , ^{11}C and ^{15}O is 109.8 minutes, 20.4 minutes and 2.0 minutes, respectively. A good PET radiotracer is one with a long enough half-life to allow enough time for imaging, while not being too long that it will stay radioactive for a long time after the imaging is finished. In this respect, ^{18}F and ^{11}C are good PET radiotracers with ^{15}O being challenging due to its short half-life.

1.2 PET Instrumentation

PET imaging scanners consist of many γ -ray detectors coupled to signal amplification and readout devices. The γ -ray detectors of choice for PET imaging are scintillation crystals: these are inorganic crystals that emit visible (scintillation) light when γ -ray photons interact with it. A photo-detector and amplification device is then used to detect the scintillation photons. These components are then arranged in a configuration that optimizes the detection of nearly collinear γ -ray photons. Most PET systems use a ring or polygonal detector configuration as shown in see Figure 1.1. The rings or polygons can then be stacked side-by-side to provide larger solid angle coverage and allow for 3D imaging.

¹ The SI units of activity is the Becquerel (Bq), with 1Bq = 1 decay/second.

The scintillation crystals have high effective atomic numbers and high density to provide a high stopping efficiency for 511 keV photons and increase the probability of detection. The scintillation process produces lower energy scintillation photons (usually in the ultraviolet range at ~400 nm) that can then be detected by the appropriate photo-detector. Scintillation photons are produced at a specific rate for each crystal type and have a characteristic exponential decay with a decay constant usually in the range of tens or hundreds of nanoseconds. Since we are interested in detecting pairs of γ -ray photons hitting the detectors at the same time, a low decay constant is desired to avoid mislabeling background photons as true pairs. The number of scintillation photons produced should ideally be large and proportional to the energy deposited within the crystal. This helps to improve the energy resolution of the crystal and allows for efficient rejection of low energy photons that may be produced by scattering within the object being imaged. In order to increase resolution and control the light distribution within the crystal, a series of fine cuts of varying lengths (*lightguides*) are made within each crystal block to divide them into smaller individual elements.

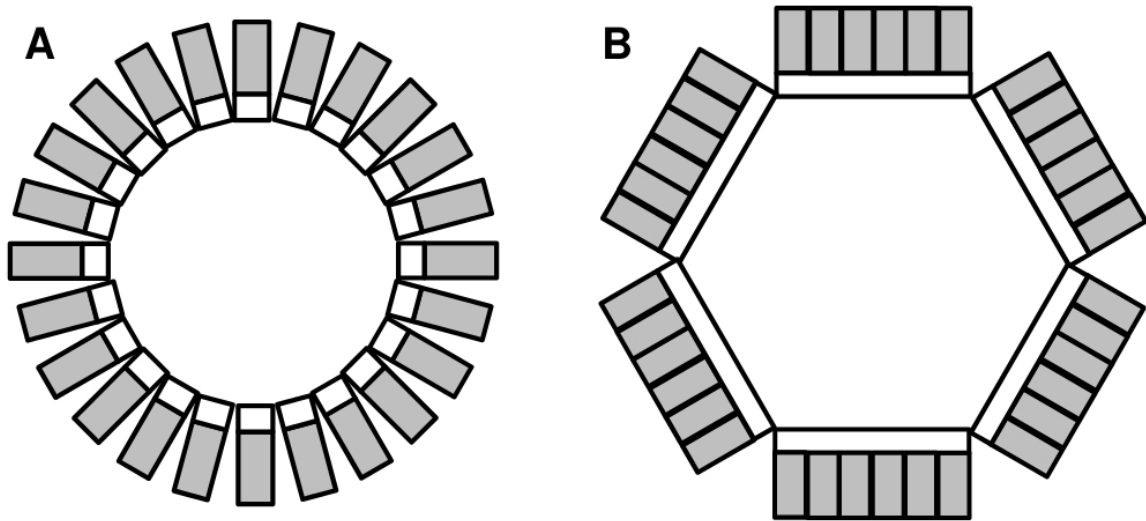


Figure 1.1: Sample configuration for PET detectors using a ring (A) and hexagonal (B) geometry. Scintillation crystals can be designed in small elements (A) or larger continuous elements (B).

Typical scintillation crystals used in PET are bismuth germanate ($\text{Bi}_4\text{Ge}_3\text{O}_{12}$, BGO), lutetium oxyorthosilicate doped with cerium ($\text{Lu}_2\text{SiO}_5:\text{Ce}$, LSO) and lutetium-yttrium oxyorthosilicate doped with cerium ($\text{Lu}_{1.8}\text{Y}_{0.2}\text{SiO}_5:\text{Ce}$, LYSO). The last two scintillators provide a good all-around performance (high density, short decay constant, reasonable energy resolution) and are used in many new PET systems (Nutt, 2002; Townsend, 2004).

The photo-detectors commonly used for PET are photo-multiplier tubes (PMTs) and semiconductor-based photodiodes. PMTs have been in use the longest and represent the most common photo-detector for PET, while photodiodes are a new technology that is rapidly improving. PMTs are devices operating at vacuum which produce electrons in a photocathode by interacting with scintillation photons. The electrons are then accelerated in a series of electrodes with increasing voltages, resulting in the production of additional electrons at each electrode (see Figure 1.2A). This creates a high amplification of the signal that is detected at the anode as a sharp pulse of high current. A one-to-one coupling of the scintillation crystal elements and PMTs is not commonly used due to the high cost and complexity of this design. Instead, a block detector design is used (see Figure 1.2B), where crystal elements are much smaller than the size of the PMTs, multiple crystal elements share a few PMTs and Anger logic is used to find the location of the crystal element associated with each event (Bailey, 2005).

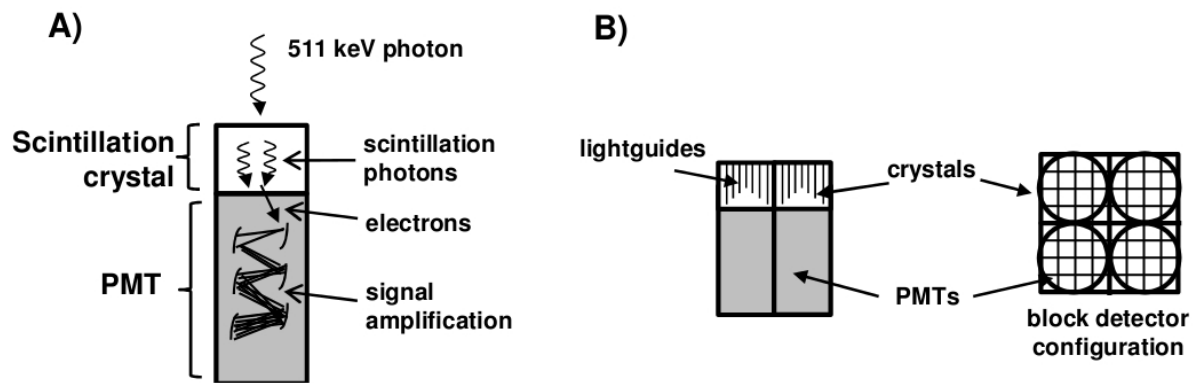


Figure 1.2: A) Schematic of PET detectors consisting of scintillation crystals and PMTs. B) Block detector configuration with many crystal elements (separated by lightguides) sharing a few PMTs.

The spatial resolution of PET scanners is determined by a number of factors, such as the positron range in the object being imaged, the non-collinearity of the γ -ray photons, the size of the individual crystal elements, and the algorithm used to find the location of the event (Moses et al., 1997). The non-collinearity of γ -ray photons arises from the fact that the $\beta\beta^+$ pair might not be at rest during annihilation and conservation of momentum results in deviations from 180° between the photons. The range of possible deviations has been found to be described by a Gaussian with a full-width at half maximum (FWHM) of about 0.5° (Shibuya et al., 2007). For a detector 20 cm away from the annihilation site this translates to a degradation in the spatial resolution of ~ 1 mm.

The PET scanner used for the work presented in this dissertation is the CTI/Siemens ECAT High Resolution Research Tomograph (HRRT). It consists of eight flat panels of crystal material arranged in an octagonal configuration. Each panel is 175mm wide and 252 mm in length with 117 detector blocks arranged in a 9×13 array coupled to a 10×14 array of PMTs in a block design (de Jong et al., 2007). The detector blocks consist of two crystal layers with LSO on the front and LYSO at the back and each block has 8×8 individual crystal elements (each element is 2.1×2.1 mm), resulting in 4 PMTs for each crystal block. The axial field of view (FOV) is 25.2 cm long and the transaxial FOV is 31.2 cm in diameter. The small crystal elements and use of double-layered high performance scintillation crystals allows this scanner to have a high sensitivity throughout the FOV and a very high spatial resolution of ~ 2.4 mm (Sossi et al., 2005; de Jong et al., 2007). This scanner is therefore ideal for dedicated human brain imaging and was used to collect all PET data in this dissertation.

1.3 Data Acquisition

PET data is collected by measuring temporal coincidences: pairs of γ -ray photons detected within a small coincidence time window (usually a few nanoseconds) at two opposing detector elements. The imaginary line connecting the two detector elements is called the line of response (LOR) and can be described by the distance of the LOR from the center of the FOV (r), the transaxial angle of the LOR (θ), the azimuthal angle (φ) and the axial position of the middle of the LOR (z) as shown in Figure 1.3. The intersection of multiple LORs will

then correspond to the location within the scanner where all the detected photons were created, thus registering coincidence events.

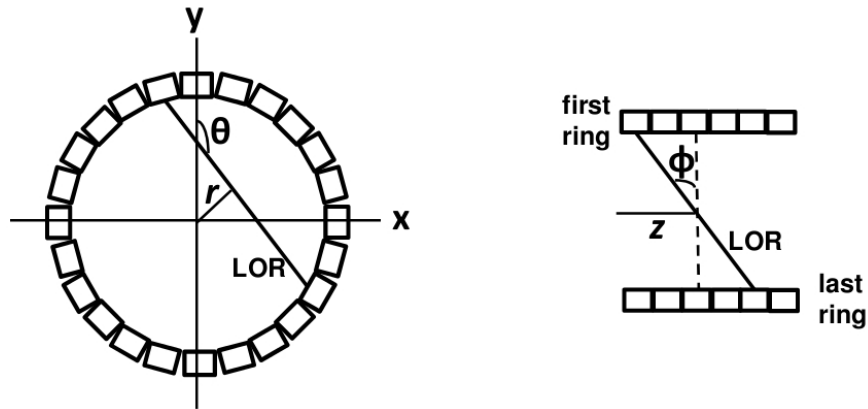


Figure 1.3: Schematic showing the LOR parameters ($\mathbf{r}, \theta, \phi, \mathbf{z}$) from a transaxial (left) and axial (right) view.

The data that are collected can be stored in sinogram or listmode formats. Sinograms are 2D histograms of the number of events detected at each LOR over the allowed range of transaxial angles (θ) and distances along the FOV (r). We can also think of sinograms as a series of 1D projections, $p(r, \theta)$, of the object being imaged taken over the allowed range of transaxial angles. A sample sinogram for a point source is shown in Figure 1.4. For 3D data, a sinogram can be created for each azimuthal angle (ϕ) that is present in the data and its associated axial position (z). An appropriate mathematical algorithm can then be used to reconstruct the original 3D spatial distribution from the sinograms. In order to incorporate time information (also called *dynamic* scanning), data are collected for a specific amount of time, stored into a series of sinograms and the process repeated until the end of the imaging session.

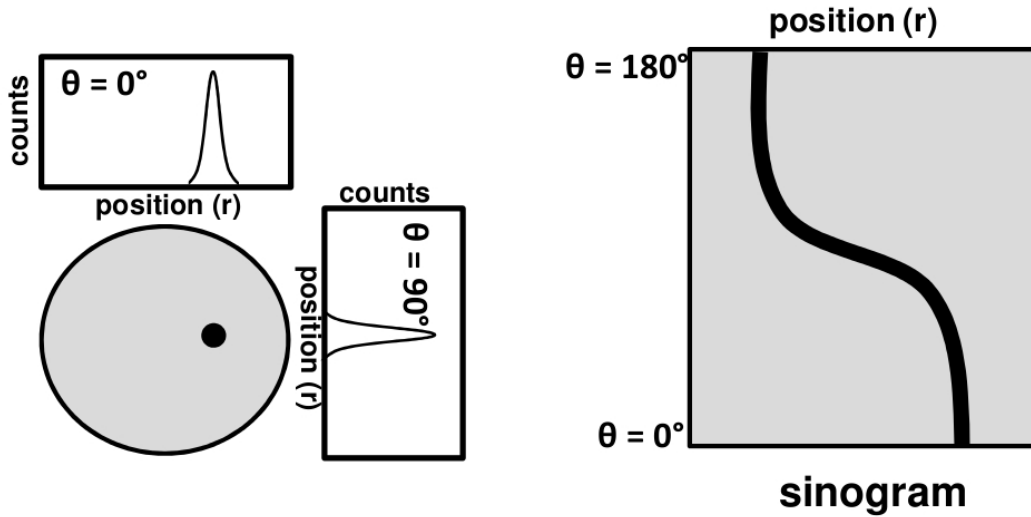


Figure 1.4: *Left – sample projections of a point source at two different transaxial angles. Right – Corresponding sinogram.*

Alternatively, data can be stored in listmode format. Here, information about each coincidence event detected is stored individually. The information can be in the form of two identifications corresponding to the detector elements which detected the coincidences or the four LOR parameters (r, θ, φ, z) described above. Time information about when the coincidences were detected is included by writing time stamps into the list-mode file at specific intervals (usually in the order of a millisecond). Each coincidence event is then associated with the closest time stamp in order to have temporal information. Other information that can also be recorded is the energy deposited by each photon and their relative detection times. Listmode data are therefore very flexible in that data can be grouped using various criteria after detection and as needed by the analysis being carried out (data can be grouped according to specific energy boundaries, time frames, etc). In sinogram format, these parameters need to be pre-determined before the imaging session and cannot be changed while imaging is taking place. On the other hand, listmode data can require large amount of disk space for storage.

1.4 Data Corrections

A series of corrections need to be applied to PET data for accurate quantitative studies. The coincidences detected by PET scanners are not only “true” coincidences, but can be random and scattered coincidences (see Figure 1.5). True coincidences are those that occur when both photons from an annihilation event are detected as coincidences, in this case neither photon undergoes any form of interaction before being detected and no other event is detected within the coincidence time window. True coincidences can be lost to attenuation (see below) due to photon interactions with matter inside the scanner (e.g., the object being imaged) or scattering into angles outside the FOV. Corrections to account for the differences in detector efficiency between detector elements and patient motion during the scan can also be made.

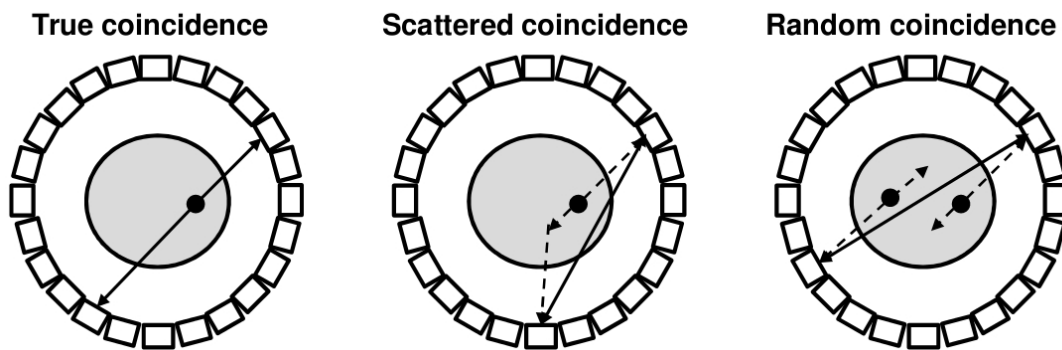


Figure 1.5: Sample schematic showing true (left), scattered (center) and random (right) coincidences detected by PET systems.

Scatter coincidences arise when one or both of the photons have undergone at least one Compton scattering before being detected. Compton scattering results in a reduced photon energy and a change in the photon direction, producing an incorrect LOR for the coincidence. The amount of scattered photons detected can be reduced by rejecting photons that lie outside an energy window centered on 511 keV. Several other methods have been used to correct for scatter, including the use of multiple energy windows and the use of a physical model to describe the scattering process (Watson et al., 2004)

Random coincidences are created by two photons which do not originate from the same annihilation event but are detected as a coincidence pair by chance. The rate at which these coincidences occur depends on the rate at which single events are detected (events where the second photon is not recorded due to attenuation, scatter, or non-interactions with the detector elements). For each LOR m , the expected number of random coincidences (r_m) collected within an imaging time Δt can be estimated using the rate of single events recorded by the two detectors (R_i and R_j) within the coincidence time window (2τ) as $r_m = 2\tau R_i R_j \Delta t$. This requires an estimate of the singles rates R_i and R_j . The number of random coincidences can also be estimated by introducing a time delay into the coincidence window, which will detect events that have zero probability of arising from a true coincidence and instead arise by chance.

The loss of photons due to attenuation is a serious concern for PET data, where imaging of human subjects can lead to a loss of over 90% of the photons for some LORs (especially for those passing through a large amount of dense material). Attenuation in this case is mostly due to Compton scattering where one of the two photons is not detected. Since we are dealing with two photons, the attenuation does not depend on the location along the LOR where the annihilation occurs but only on the total amount and type of attenuation material. Attenuation can be corrected for each LOR by estimating the probability, P , that the photon will not interact with the material along the LOR as given by $P = \exp\left(-\int_{LOR} \mu(x) dx\right)$. Here, $\mu(x)$ is the linear attenuation coefficient of the material at position x along the LOR. One method to correct for attenuation is to estimate the values of $\mu(x)$ within the image, also called a μ -map. This is done by using an external radiation source (*transmission source*) to produce two sets of sinograms: one of the transmission source while the scanner is empty (a *blank scan*) and one of the source while the object being imaged is placed inside the scanner (a *transmission scan*). The ratio of *blank scan/transmission scan* can then be used to estimate the amount of attenuation present for each LOR and thus a μ -map. The μ -map can then be used to correct the PET image of the object. Additional methods to correct for attenuation involve estimating attenuation from fixed anatomy models (e.g., an average head anatomy) and using computed tomography (CT) or magnetic resonance (MR) images to derive μ values (Bailey, 2005; Hofmann et al., 2009).

In addition, variations in the production and individual characteristics of each detector element in the PET scanner will cause variations in their sensitivity as high as 10% or more. Differences in the geometrical positions of two detectors contributing to an LOR will also contribute to detector variations in the scanner. A correction for this effect (called *normalization*) can be made by exposing the detector to a well-known source of radioactivity. Differences between the expected and detected count rates for each LOR can then be used to correct for differences in detector sensitivities. The effect of subject motion can also affect the data collected as it will contribute to degradation of spatial resolution. In order to reduce this effect, an individually molded thermoplastic mask can be used for every subject, the amount of motion can be measured using an optical tracking device (Bloomfield et al., 2003) and/or the images obtained during the scan can be realigned with a suitable algorithm (Dinelle et al., 2011).

1.5 Image Reconstruction

After data have been collected, the coincidences recorded for each LOR have to be reconstructed into a 3D image. The algorithms commonly used for this purpose can be divided into analytical and iterative algorithms. In this section we review the key characteristics of each.

The most common analytic reconstruction algorithms are those based on backprojection techniques. Here, the counts collected for each projection $p(r, \theta_i)$ at angle θ_i are uniformly distributed along the imaging space $f(x, y)$. This process (called *backprojection*) is repeated for every angle θ_i along which data were collected. If the angles were sampled uniformly around the entire object there is enough data to accurately reconstruct the entire image volume. One of the drawbacks with this technique is that part of the detected counts are always projected outside the object being imaged, resulting in a blurring effect. Blurring can be thought of as increased signal present at large spatial dimensions or, in frequency space, increased signal at low frequencies. This blurring can be decreased by *filtering* the data before backprojecting. The most common analytic reconstruction technique involves computing the Fourier Transform of each projection, multiplying by a filter that decreases

signal at low frequencies, computing the Inverse Fourier Transform of the resulting projection and then backprojecting the filtered profiles. This is known as a *filtered backprojection* (FBP) and is the most widely used reconstruction technique. While this procedure is fast and easy to implement, the resulting images still suffer from large amounts of noise, reduced resolution and various reconstruction artifacts. In addition, the FBP algorithm cannot be modified to take into account physical processes affecting the data and properties of the imaging system, such as scatter, attenuation, differences in detector sensitivities and more. Such effects need to be taken into account in pre- or post-processing steps with varying degrees of success.

Iterative methods are used when more flexibility is needed in the reconstruction process. The general concept of iterative reconstruction is shown in Figure 1.6. The goal is to arrive at the best estimate of the true image by successive approximations. The process is started by providing an initial estimate of the image and producing estimated projections by *forward projection*. As the name suggests, this is exactly the opposite of backprojection and is carried out by summing the counts in the estimated image over all required angles. The set of estimated projections, $p'(r, \theta)$ are then compared to the actual measured projections $p(r, \theta)$ and the differences between them are used to update the image estimate. The process is then repeated for a specific number of iterations or until the differences between the estimated and measured projections drops below a predetermined threshold level. One of the key strengths of iterative algorithms is their ability to incorporate corrections into the reconstruction process, by taking into account physical processes and imaging system characteristics in the forward projection step. At the same time, these properties make iterative algorithms much slower and computationally demanding to run than FBP. One method that has been developed to speed up the algorithms is to only use a subset of the available projections during each iteration. An example of this method is the ordered subset expectation maximization (OSEM) algorithm, which incorporates statistical information to compute the most likely source image using a subset of projections in each iteration.

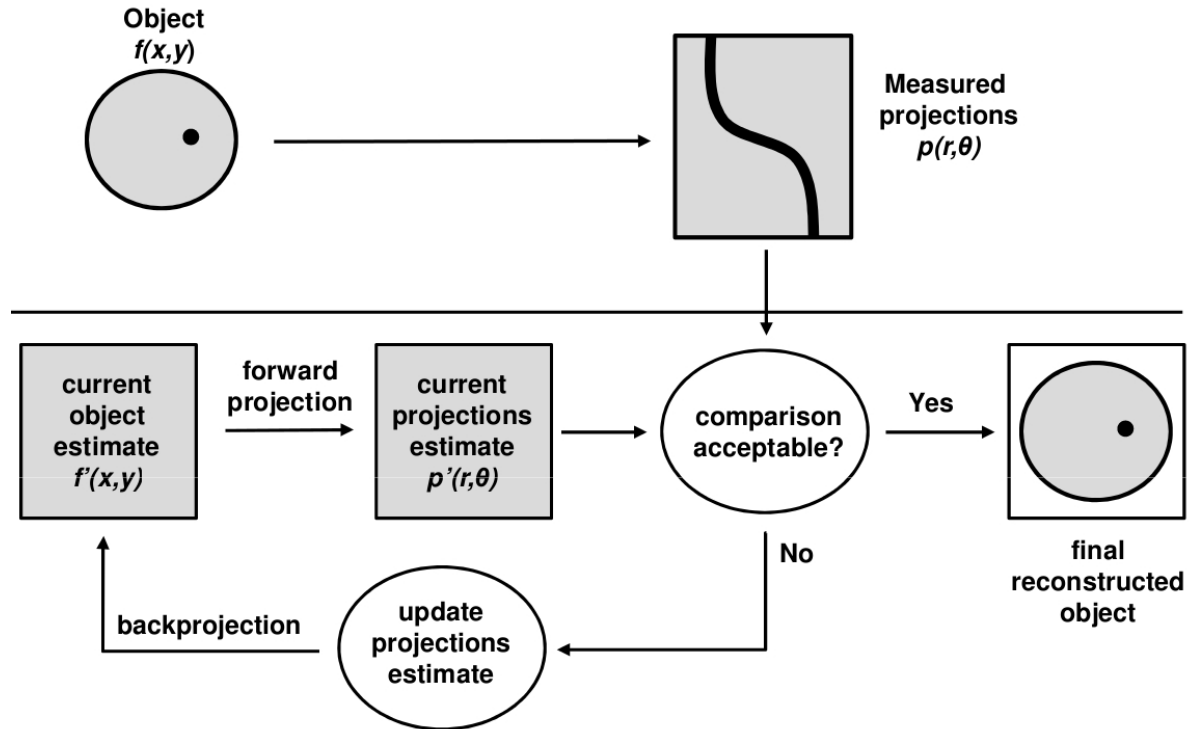


Figure 1.6: Schematic summary of the key steps in iterative reconstruction.

1.6 Data Analysis: Kinetic Modeling

PET imaging over a period of time allows us to study how the concentration of the radiotracer changes over time and therefore provides information about the *functional* properties of the body. We can then use a mathematical model to derive parameters that describe how the tracer interacts in the body as a function of time (*kinetic modeling*). Using kinetic modeling we can derive quantities that are related to the strength of the binding between the tracer and its target cells and the rate at which the tracer is taken up, used or released by cells. For example, the radiotracer FDG is used to estimate the rate of glucose use in the body and has been proven to be helpful in detecting fast-growing cancer cells that use glucose as a source of fuel.

Kinetic modeling involves developing a biological model for how the tracer interacts in the body. This is usually done by assuming that the tracer will flow between different

compartments, which are described as volumes where the tracer will be uniformly distributed. Compartments can be open or closed depending whether the tracer is allowed to escape the compartment or not. Compartments do not necessarily have a simple biological meaning since depending on the tracer it can be taken up by one specific cell type in a specific organ or many cells in different organs. Therefore, a kinetic model for each tracer needs to be developed according to the specific physiological and biochemical principles that govern the tracer's interactions in the body. Mathematical kinetic models then describe the rate of exchange of the tracer between different compartments (through *rate constants*) and the amount of tracer concentration present in each compartment. These models are commonly formulated using differential equations.

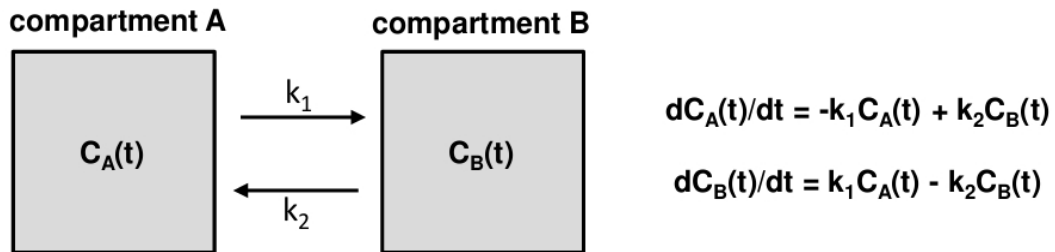


Figure 1.7: Simple two-compartment kinetic model with rate constants k_1 and k_2 and concentrations in each compartment of $C_A(t)$ and $C_B(t)$.

A simple two compartmental model with its associated equations and parameters is shown in Figure 1.7. Here, the concentration of the tracer over time in compartment A, $C_A(t)$, is commonly called the *input function*. The concentration of the tracer over time in compartment B, $C_B(t)$, is what we measure with a time-series of PET images and generally represents the amount of tracer over time in the tissue of interest. To measure $C_B(t)$ we select a region of interest (ROI) in the PET images where the tissue of interest is located, we then extract the observed number of counts within the ROI in the PET images and plot them as a function of time. The resulting plot is known as a time activity curve (TAC). In order to estimate the rate constants (in this case k_1 and k_2) that describe the tracer kinetics, we need an estimate of both the input function and $C_B(t)$. The input function can be obtained by taking arterial blood samples throughout the scanning session, which is not always possible

and can sometimes be very challenging for patients. On the other hand, the input function can be estimated by using another region within the PET image (called *reference region*) where the tracer has negligible specific binding². TACs derived for the tissue and reference regions are then used to solve the differential equations of the kinetic model being used. A sample set of TACs is shown in Figure 1.8.

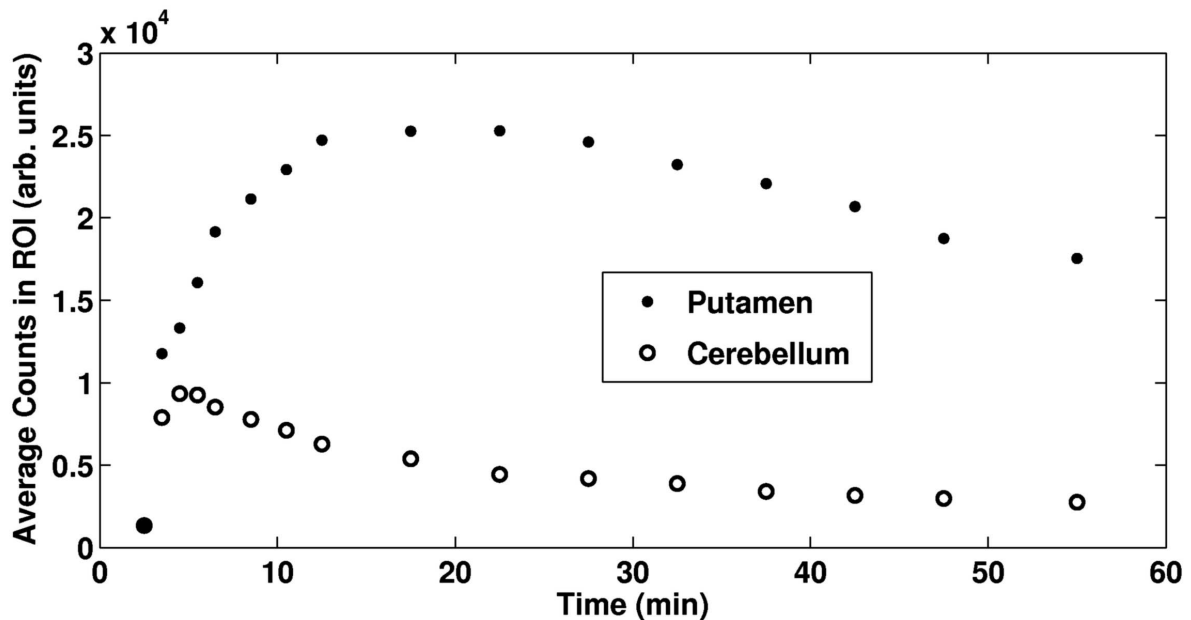


Figure 1.8: Sample TACs for the putamen (tissue of interest) and the cerebellum (reference tissue) using the radiotracer [¹¹C]Raclopride.

Every radiotracer behaves differently in the body and it could also behave differently in different tissues. Therefore, the specific model used (number of compartments and rate constants) has to be characterized individually for each tracer in each tissue of interest and reference region. A sample three compartmental model with a reference region that includes tracer flow from/to plasma is shown in Figure 1.9. Tracers are generally described as being *reversible* if they can become bound and unbound in the tissue of interest. On the other hand,

² Tracer binding to the tissue of interest is called *specific binding*, while binding to other sites is called *nonspecific binding*.

tracers are described as irreversible if they remain bound ($k_4 = 0$ in this example). For reversible tracers, the parameter of interest for this dissertation is the tracer's *binding potential* (in this example k_3/k_4), which can be interpreted as representing the number of available sites where the tracer can become bound (also called B_{max}) divided by the rate at which the tracer becomes unbound (also called the dissociation constant, K_D). This approach is used to find the non-displaceable binding potential (BP_{ND}) of radiotracers such as [^{11}C]Raclopride and [^{11}C]Dihydrotetrabenazine (see Section 3.4). For irreversible tracers, we are interested in the rate at which the tracer is taken up in the tissue of interest, also called the *uptake rate*. When a reference region is used to study the kinetics of the tracer (as in our example), the uptake rate can be defined as $k_2k_3/(k_2+k_3)$ (Patlak and Blasberg, 1985). This approach is used to find the dopamine uptake rate constant ($K_{occ} = k_2k_3/(k_2+k_3)$) using the radiotracer [^{18}F]Fluoro-L-dopa (see Section 3.4).

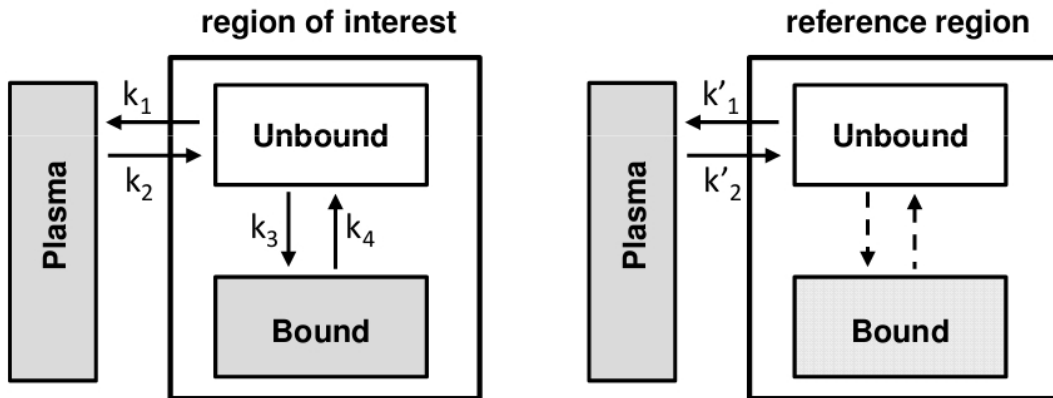


Figure 1.9: Kinetic model using a reference region as the input function.

In addition to applying kinetic modeling to the TACs derived by averaging concentrations from ROIs within the image, they can be applied to individual voxel TACs. The derived kinetic parameters can be used to make a *parametric image* of the values for every voxel. These parametric images can then be used to study all regions of the brain without preselecting regions of interest. However, this method is very sensitive to noise in the original image and noise-induced biased can be very important in the derived kinetic parameters.

1.7 MRI Basics

Magnetic resonance imaging (MRI) is a medical imaging technique that also allows us to study the human body *in vivo* (Chakeres and Schmalbrock, 1992). While PET is used to study the functional properties of the body, for the purpose of this dissertation MRI will be used to study the structural (also called *anatomical*) properties of the body in order to locate anatomical regions of interest in the body. In this way, MRI provides complementary information about the body than that available with PET imaging.

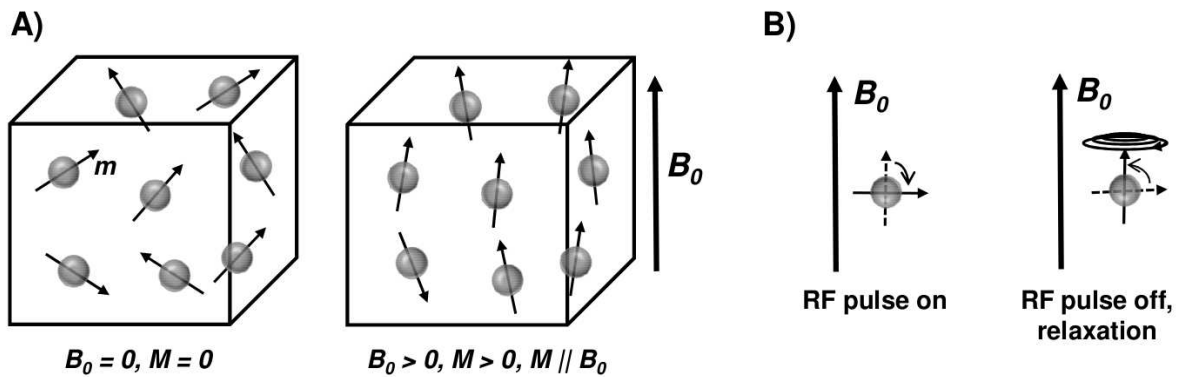


Figure 1.10: A – Schematic showing alignment of nuclear magnetic moments in the presence of an external magnetic field (B_0). B – Use of an RF pulse to flip spins and their subsequent relaxation.

The basic principle of MRI relies on the fact that the body contains a large amount of protons (mostly present in hydrogen nuclei inside water molecules), which in turn have a magnetic moment, m . Normally, the nuclear magnetic moments have random orientations inside the body (see Figure 1.10A). However, when the body is placed inside a large magnetic field (B_0), the hydrogen nuclei align themselves with the direction of the magnetic field and can combine to create a macroscopic magnetic moment (M). In order to produce a signal from M that can be observed it is necessary to disturb the system. The magnetic moment will be able to absorb energy at a specific frequency, called the *Larmor frequency*, given by:

$$\omega_0 = \gamma B_0, \quad (1.2)$$

where $\gamma=42.6$ MHz/T for a proton. A radio frequency (RF) coil is therefore used to transmit a pulse with a frequency ω_0 into the body for a brief period of time which will cause the magnetization to tilt away from B_0 and precess around it. As it precesses, the magnetization will create a current on the RF coil by Faraday induction which is then detected by a receiver coil. Once the RF pulse is turned off, the magnetization will realign itself with B_0 within a characteristic time (called *relaxation time*, see Figure 1.10B). The longitudinal component of the magnetization (parallel to B_0) relaxes due to spin-lattice interactions with a characteristic time generally known as T1. The transverse component of the magnetization (perpendicular to B_0) relaxes due to spin-spin interactions with a characteristic time generally known as T2. For a given input RF pulse, nuclei in different body tissues will have different relaxation times which will change the RF signal received from them and allows MRI to provide contrast between different tissue types. In order to produce a 3D image of the body, the magnetic field is changed by the use of gradient coils so that it varies in all three spatial directions, $B_0(x, y, z)$. In this way, the RF signal received will have a spatially-varying frequency profile which can be mapped into a grid called *k-space*. An inverse Fourier transform of this signal can then be used to remap the spatial frequencies into spatial coordinates.

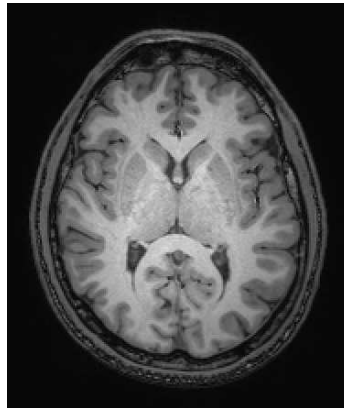


Figure 1.11: Sample T1-weighted MR image.

The contrast in a MR image can be manipulated by changing the parameters of the input RF pulse and the gradient coils. In particular, the RF pulse can be repeated at specific intervals

with a period called the *repetition time* (TR). We can also manipulate the gradient coils in order to change the time at which the signal is received after the RF pulse is sent, called the *echo time* (TE). Since different tissues will have different $T1$ and $T2$ relaxation times, adjusting TR and TE accordingly allows us to give different contrast to different tissues as needed. For example, a so-called $T1$ -weighted image will use a short TR and short TE resulting in images where tissues that have different $T1$ values will have different contrast (the areas with shortest $T1$ values will show as the brightest regions in a $T1$ -weighted image). For example, Figure 1.11 shows a $T1$ -weighted image with $TR = 7.6$ ms and $TE = 3.5$ ms where white matter ($T1 \sim 700$ ms, $T2 \sim 90$ ms) has bright signal, grey matter ($T1 \sim 800$ ms, $T2 \sim 100$ ms) is darker, and the ventricles with large amounts of water ($T1 \sim 3000$ ms, $T2 \sim 3000$ ms) are very dark.

1.8 Thesis Motivation and Outline

As described in Section 1.6, the quantitative analysis of PET data traditionally involves kinetic modeling of the concentration of the radiotracer over time. This modeling is used to derive parameters related to the binding/uptake of the radiotracer in the body. While this analysis is very common it is not trivial to perform. On the other hand, relatively little work has been done in assessing the information about functional processes that can be gained from the spatial distribution of the radiotracer. While the spatial resolution available in most human PET systems (~ 3 - 6 mm) is lower than that available in other medical imaging modalities (down to sub-mm for magnetic resonance imaging – MRI), it is worthwhile to investigate the use of spatial information from PET data, especially with the higher resolution available in modern scanners (de Jong et al., 2007; Delso et al., 2011).

The most common approach to investigate spatial information in human brain imaging involves warping each individual image to a common template (Ashburner and Friston, 1997; Brett et al., 2002). This method allows the comparison of images from different subjects at the voxel level with the goal of reducing intersubject anatomical variability. However, this method is very susceptible to misregistration errors given the substantial anatomical variability between individuals and a high degree of spatial smoothing is

commonly used to overcome this problem. The resulting warped images have degraded spatial information and residual misregistration errors can still reduce the amount of functional overlap between subjects (Gispert et al., 2003). Nonetheless, this technique has been used for PET studies and has proven insightful. For example, relative differences in radiotracer binding between different brain areas (e.g., low binding in frontal lobe) have been related to cognitive decline and used to study various forms of dementia (Ishii et al., 2001; Ercoli et al., 2012).

Alternatively, we can extract data within a specific ROI for each subject and compare spatial characteristics across subjects within the ROI. In this case, the original information in the image and the spatial resolution are maximally preserved. The main problems with this method are: a) defining the ROI consistently for all subjects, and b) using an analysis method that does not amplify intersubject variability. ROI definition can be a challenge and is usually derived from an anatomical image using previous neuroanatomy knowledge (Mitsis et al., 2008). Despite the variability that this ROI definition introduces, in certain cases it has been shown to produce better localization and higher sensitivity than whole brain warping (Nieto-Castanon et al., 2003; Ng et al., 2010). In the case of PET data, where anatomical information is limited, ROI definition is especially challenging. The availability of multimodality scanners (PET/CT and PET/MRI) will help in developing a consistent method for ROI delineation (Delso et al., 2011).

The focus of this dissertation is then to investigate a novel, subject-specific, ROI-based analysis method for PET data that characterizes the radiotracer spatial distribution and is minimally affected by intersubject variability. In other words, we would like to study the radiotracer's spatial distribution within an ROI containing, for example, the putamen, while being minimally affected by individual differences in putamen size and image orientation. In tumor imaging, recent PET studies have shown that using the spatial characteristics of tumors (also referred to as tumor heterogeneity) can enhance predictions of response to therapy (Tixier et al., 2011), treatment outcomes (El Naqa et al., 2009), and survival (Eary et al., 2008).

This work then investigates the use 3D moment invariants (3DMIs) to quantify spatial characteristics in the shape and texture of PET data within a specific ROI. 3DMIs are

mathematical shape descriptors designed to be unchanged (*=invariant*) to scaling, translation and rotation (Hu, 1962; Flusser et al., 2009). 3DMIs are combinations of terms describing the variance, skewness and kurtosis of a distribution and can be thought of as measuring deviations from a smooth and symmetric 3D spatial distribution. 3DMIs quantify not only the 3D shape of an object (as defined by its outer boundaries) but also the 3D spatial distribution of voxel values within the object (also called its “texture” or “heterogeneity”). The hypothesis of this work is that 3DMIs will be able to describe the spatial distribution of a radiotracer within a specific ROI in a PET image. In addition, this work will test whether 3DMIs are able to differentiate between healthy and pathological states where the spatial distribution of radioactivity within an ROI is changed as a consequence of disease. Spatial information can then be added to parameters derived from kinetic modeling to increase the information gained from PET imaging about pathological states. In order to test these hypotheses, 3DMIs were applied to PET images of healthy controls and subjects with Parkinson’s disease (PD). In addition, we will use anatomical MR images to determine the ROIs appropriate for this work.

This dissertation is then divided as follows: Chapter 2 summarizes the construction and properties of moment invariants starting in 2D and expanding the results to 3D; Chapter 3 provides an introduction to PD, its clinical features, the dopaminergic brain system involved in it and the role of PET imaging in the disease; Chapter 4 describes the methodology and results obtained when applying 3DMIs to PET images of healthy controls and subjects with PD; finally, Chapter 5 provides the conclusions derived from this work and the future directions that can be followed.

Chapter 2: Moment Invariants

2.1 Introduction

Deriving a mathematical way to describe the shape of an object and classifying it accordingly is extremely useful. The shape of an object being imaged can be used to recognize and classify it according to its spatial properties. In medical imaging, we require a mathematical shape descriptor that does not change (ie, remains *invariant*) for subjects of different physical sizes and different orientations while they are being imaged. The shape descriptor should then be invariant to geometrical changes such as scaling, translation and rotation of the object. However, we also require that this descriptor is able to *discriminate* between objects of different shapes so that real underlying differences between subjects can be found. An appropriate balance between invariance and discriminate power is therefore needed.

Here we give a general introduction to the mathematical shape descriptors known as *moment invariants*. 2D moment invariants have been used in pattern recognition and image processing since first introduced by (Hu, 1962), who used group theory to derive the required expressions. The 3D versions of these invariants were first introduced by (Sadjadi and Hall, 1980) and have been expanded by others (Galvez and Canton, 1993; Guo, 1993). Moment invariants have become one of the most important and most frequently used shape descriptors with wide ranging applications in object recognition (Flusser et al., 2009). In order to describe moment invariants the concept of *moments* will be introduced first, as well as a description of how they are used to characterize functions and distributions. Moment invariants are then formulated by combining moments in specific ways to achieve invariance to translation, scale and rotation. For a detailed introduction to moments, moments invariants and their application to pattern recognition and image analysis see (Flusser et al., 2009).

2.2 2D Moments

Moments are traditionally used to describe the “shape” of probability density functions and are also used to measure the mass distribution of a body. For a 2D distribution given by $f(x, y)$, in our case this can describe a 2D image, the moments of order $n=p+q$ are given by:

$$m_{pq} = \int_{-\infty}^{+\infty} \int_{-\infty}^{+\infty} p(x, y) f(x, y) dx dy = \int_{-\infty}^{+\infty} \int_{-\infty}^{+\infty} x^p y^q f(x, y) dx dy . \quad (2.1)$$

The last expression on the right describes the *geometric moments* since they are calculated by “projecting” $f(x, y)$ onto the polynomial basis given by $p(x, y) = x^p y^q$. These represent the most common moments used. Different basis functions are also possible, e.g., using $p(x, y) = (x + iy)^p (x - iy)^q$ gives rise to *complex moments*.

Geometrical moments are simple and generally easy to understand, at least at low orders m . For example, zeroth and first order moments can be combined as follows:

$$m_{00} = \int_{-\infty}^{+\infty} \int_{-\infty}^{+\infty} f(x, y) dx dy , \quad (2.2)$$

$$\frac{m_{10}}{m_{00}} = \frac{\int_{-\infty}^{+\infty} \int_{-\infty}^{+\infty} x f(x, y) dx dy}{\int_{-\infty}^{+\infty} \int_{-\infty}^{+\infty} f(x, y) dx dy} = \bar{x}, \quad \frac{m_{01}}{m_{00}} = \frac{\int_{-\infty}^{+\infty} \int_{-\infty}^{+\infty} y f(x, y) dx dy}{\int_{-\infty}^{+\infty} \int_{-\infty}^{+\infty} f(x, y) dx dy} = \bar{y} . \quad (2.3)$$

Here, m_{00} can be thought of as the totally “mass” of the image (or the area of an object for 2D images) while m_{10}/m_{00} and m_{01}/m_{00} can be thought of as the “centers of mass” or *centroids* of the image. Similarly, the second order moment m_{20} and m_{02} describe the “distribution of mass” or *moments of inertia* of the image with respect to each coordinate axes. It is also helpful to think of moments as describing the shape of a probability density function represented by the image. In this case m_{00} is the sum of all values in the image, while m_{10}/m_{00} and m_{01}/m_{00} can be thought of as describing the *mean values*.

While geometrical moments are useful for describing general properties of the objects being studied, they cannot be used to characterize spatial distributions of different subjects since they are sensitive to changes in position, size and orientation. In order to derive moments that remain *invariant* in those circumstances we need to modify the moments in specific ways. As it is shown below, individual moments can be made invariant to scaling and translation on

their own, while invariance to rotation is derived by using special combination of multiple moments.

2.2.1 Invariance to Translation

Moments can be made invariant to translation somewhat easily by using the object centroid coordinates as the origin of the coordinate system. For the geometric moments described above we can then derive the *central geometric moments* which are invariant to translation as follows:

$$M_{pq} = \int_{-\infty}^{+\infty} \int_{-\infty}^{+\infty} (x - \bar{x})^p (y - \bar{y})^q f(x, y) dx dy , \quad (2.4)$$

where the centroid coordinates are found using Equation 2.3. These moments are then invariant to the translation of the object within the imaging area.

Here, second order central moments represent the variance along each axis (M_{20} and M_{02}) as well as the covariance between two axes (M_{11}). In this way, second order central moments can be used to define the orientation of the image. Two additional higher order moments are generally used: *skewness* and *kurtosis*. Third order central moments are used to describe the skewness of the distribution in each direction ($M_{30}/M_{20}^{3/2}$ and $M_{03}/M_{02}^{3/2}$), where skewness is used as a measure of deviations from symmetry in the distribution. In addition, fourth order central moments are used to describe the kurtosis of the distribution (M_{40}/M_{20}^2 and M_{04}/M_{02}^2), which can be classically thought of as a measure of both the “peakedness” of the distribution and the heaviness of its tails. In Figure 2.1 we show distributions that demonstrate the characteristics described by each of these spatial descriptors.

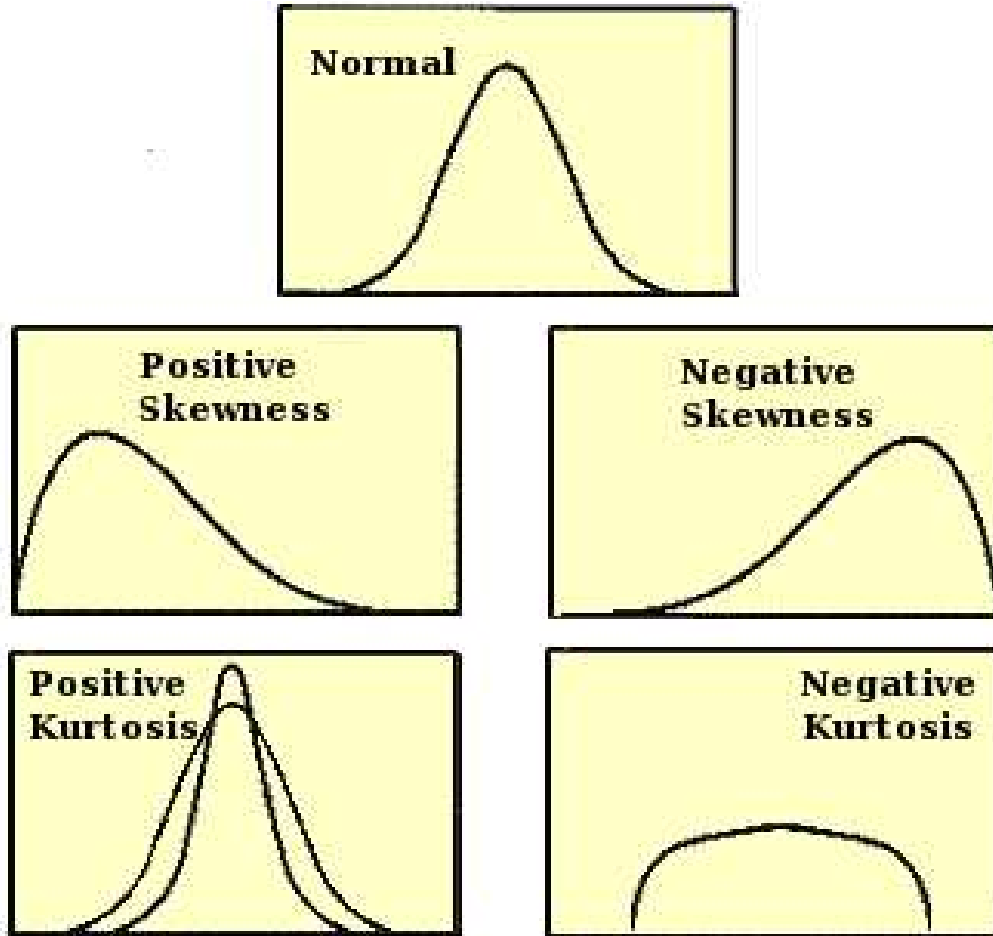


Figure 2.1: Sample distributions showing the shape characteristics that can be described using moments.

2.2.2 Invariance to Scaling

Central moments can be made invariant to the size of the object by normalizing them appropriately. In principle we can use any moment as a normalization factor as long as it is not zero. Since low-order moments are less sensitive to noise and easier to calculate, it is common to normalize by the smallest order moment M_{00} :

$$\eta_{pq} = \frac{M_{pq}}{M_{00}^{\frac{p+q}{2}+1}} \cdot \quad (2.5)$$

These are then called *normalized central moments*. Proving that μ_{pq} is invariant to scaling of the coordinates by a constant factor s can be done as follows:

$$M'_{pq} = \int_{-\infty}^{+\infty} \int_{-\infty}^{+\infty} [s^p(x - \bar{x})^p][s^q(y - \bar{y})^q] f(x, y) [sdx][sdy] = s^{p+q+2} M_{pq}, \quad (2.6)$$

so that the normalized central moment becomes:

$$\eta'_{pq} = \frac{M'_{pq}}{M'_{00} \frac{p+q+1}{2}} = \frac{s^{p+q+2} M_{pq}}{(s^2 M_{00}) \frac{p+q+1}{2}} = \frac{M_{pq}}{M_{00} \frac{p+q+1}{2}} = \eta_{pq}. \quad (2.7)$$

2.2.3 Invariance to Rotation

The construction of moments that are invariant to rotation is not straightforward. The first derivation of 2D moments that are invariants to rotation was done by (Hu, 1962), who used algebraic invariant theory to derive seven invariants using second- and third-order geometric moments. The first five Hu moment invariants are:

$$\begin{aligned} \varphi_1 &= m_{20} + m_{02} \\ \varphi_2 &= (m_{20} - m_{02})^2 + 4m_{11}^2 \\ \varphi_3 &= (m_{30} - 3m_{12})^2 + (3m_{21} - m_{03})^2 \\ \varphi_4 &= (m_{30} + m_{12})^2 + (m_{21} - m_{03})^2 \\ \varphi_5 &= (m_{30} - 3m_{12})(m_{03} + m_{12})[(m_{30} + m_{12})^2 - 3(m_{21} - m_{03})^2] + \\ &\quad (3m_{21} - m_{03})(m_{21} + m_{03})[3(m_{30} + m_{12})^2 - (m_{21} - m_{03})^2] \end{aligned} \quad (2.8)$$

If the replace the geometric moments, m_{pq} , by central moments, M_{pq} , or normalized moments, η_{pq} , the resulting moment invariants will be invariant to rotation, translation and/or uniform scaling. After Hu, many authors have re-derived the above 2D rotational invariants, including approaches using Fourier-Mellin transforms (Li, 1992), complex moments (Flusser et al., 2009) and other algorithms (Jin and Tianxu, 2004). Unfortunately, none of the derivations is straightforward. However, once they are formed it is easy to show they are invariant under rotation. In 2D, the rotation matrix for an angle of rotation θ is given by:

$$\begin{pmatrix} x' \\ y' \end{pmatrix} = \begin{pmatrix} \cos \theta & -\sin \theta \\ \sin \theta & \cos \theta \end{pmatrix} \begin{pmatrix} x \\ y \end{pmatrix} \quad (2.9)$$

$$\begin{aligned} \therefore x'^2 &= \cos^2 \theta x^2 + \sin^2 \theta y^2 - 2\cos \theta \sin \theta xy \\ y'^2 &= \sin^2 \theta x^2 + \cos^2 \theta y^2 + 2\cos \theta \sin \theta xy \end{aligned} \quad (2.10)$$

The rotated second-order moments are then given by:

$$\begin{aligned} m'_{20} &= \cos^2 \theta m'_{20} + \sin^2 \theta m'_{02} - 2\cos \theta \sin \theta m_{11} \\ m'_{02} &= \sin^2 \theta m'_{20} + \cos^2 \theta m'_{02} + 2\cos \theta \sin \theta m_{11} \end{aligned} \quad (2.11)$$

Therefore, for the first Hu invariant we find:

$$\varphi'_1 = m'_{20} + m'_{02} = (\cos^2 \theta + \sin^2 \theta)(m_{20} + m_{02}) = m_{20} + m_{02}, \quad (2.12)$$

which shows that the moment combination is invariant under rotation.

2.3 3D Moment Invariants

Invariance to translation and uniform scaling are easy to define in 3D by extending the definitions already used in 2D. Specifically, the 3D geometric and central moments are given by:

$$m_{pqr} = \int_{-\infty}^{+\infty} \int_{-\infty}^{+\infty} \int_{-\infty}^{+\infty} x^p y^q z^r f(x, y, z) dx dy dz \quad (2.13)$$

and,

$$M_{pqr} = \int_{-\infty}^{+\infty} \int_{-\infty}^{+\infty} \int_{-\infty}^{+\infty} (x - \bar{x})^p (y - \bar{y})^q (z - \bar{z})^r f(x, y, z) dx dy dz \quad (2.14)$$

where the centroids are again defined by:

$$\bar{x} = \frac{m_{100}}{m_{000}}, \bar{y} = \frac{m_{010}}{m_{000}}, \bar{z} = \frac{m_{001}}{m_{000}}. \quad (2.15)$$

Here, the order of the moment is given by $n = p + q + r$ and M_{pqr} is a translational invariant. In turn, invariance to uniform scaling can again be achieved by normalizing to the largest invariant:

$$\eta_{pqr} = \frac{M_{pqr}}{M_{000}^{\frac{p+q+r}{3}+1}} . \quad (2.16)$$

Unfortunately, invariance to rotation is even less straightforward to derive in 3D than in 2D. For example, spherical harmonics can be used instead of complex moments to derive the expressions. The first 3D moment invariants of second order were derived by (Sadjadi and Hall, 1980):

$$\begin{aligned} J_1 &= \eta_{200} + \eta_{020} + \eta_{002} \\ J_2 &= \eta_{200}\eta_{020} + \eta_{200}\eta_{002} + \eta_{020}\eta_{002} - \eta_{101}^2 - \eta_{110}^2 - \eta_{011}^2 \\ J_3 &= \eta_{200}\eta_{020}\eta_{002} - \eta_{002}\eta_{110}^2 - \eta_{020}\eta_{101}^2 - \eta_{200}\eta_{011}^2 + 2\eta_{110}\eta_{101}\eta_{011} \end{aligned} \quad (2.17)$$

Two other 3D rotational moment invariants were derived from third and fourth order moments using moment tensor contraction by (Reiss, T. H., 1992):

$$\begin{aligned} B_3 &= \eta_{300}^2 + \eta_{030}^2 + \eta_{003}^2 + 3(\eta_{210}^2 + \eta_{021}^2 + \eta_{201}^2 + \eta_{120}^2 + \eta_{012}^2 + \eta_{102}^2) + 6\eta_{111}^2 \\ B_4 &= \eta_{400}^2 + \eta_{040}^2 + \eta_{004}^2 + 4(\eta_{310}^2 + \eta_{031}^2 + \eta_{301}^2 + \eta_{130}^2 + \eta_{013}^2 + \eta_{103}^2) + \\ &\quad 6(\eta_{220}^2 + \eta_{022}^2 + \eta_{202}^2) + 12(\eta_{211}^2 + \eta_{121}^2 + \eta_{112}^2) \end{aligned} \quad (2.18)$$

In addition, (Lo and Don, 1989) presented a systematic approach to derive 3D rotational invariant moments using group representation theory and complex moments. They were able to derive a total of twelve 3D moment invariants using second and third order moments. Their results are equivalent to those shown in Equations 2.17 and 2.18 and expand on them.

Physically, the above definitions of 3DMIs can be interpreted as follows: J_1 represents the total spatial variance in the object, J_2 and J_3 incorporate spatial covariance as well as variance, while B_3 and B_4 include skewness and kurtosis, respectively, as well as other spatially descriptive terms. Although higher-order moments can be used they are more sensitive to noise and only relatively low-order moments will be used for this dissertation dealing with an initial exploration of 3DMIs for PET data.

2.4 Applications in Medical Imaging

The following are sample applications of moment invariants for the purpose of medical imaging.

Brain Morphometry: (Mangin et al., 2004) used various shape descriptors, including the 3D moment invariants of Lo and Don, to describe the shape of sulci (folds) in the brain and various deep-brain regions from MR images. They found that moment invariants are able to describe the shape of brain regions with similar structures having similar invariant values (such as the globus pallidus and putamen). They also found that moment invariants are able to find differences in the shape of brain regions according to subjects' handedness and sex. For example, they found that the collateral sulcus has a different shape, in particular a different curvature, in females and males. In contrast, the overall size of the sulcus did not show a significant difference.

Intracranial aneurisms: Intracranial aneurisms are dangerous enlargements of cerebral arteries, most commonly those that meet at the Circle of Willis. Some aneurisms result in ruptured arteries and some do not. Those that rupture result in heavy hemorrhaging and have a high rate of mortality and morbidity. Therefore, accurate characterization of aneurisms between ruptured and unruptured is critical. (Millán et al., 2007) and (Valencia et al., 2010) explored shape descriptors to predict the risk of rupture of cerebral arteries in an aneurism. They found that moment invariants provide the best predictive capabilities among different shape descriptors.

fMRI activation maps: Functional MRI (fMRI) is used to map different regions in the brain to specific brain functions. This is commonly done by having subjects perform a specific task (e.g., tapping their fingers, hearing sounds) while being imaged inside an MR scanner. The analysis of this data is commonly done by calculating statistical probabilities that voxels in the image are 'activated' and thus have higher signal while the task is being performed. The statistics for all voxels in the image are then assembled into statistical maps showing regions of the brain having high probability of being activated during the task. Typically, this is done by warping the brain image of each subject so it matches a common template and allowing

for cross-comparisons between subjects to be performed. However, this method does not account for the spatial variabilities of each subject's anatomy.

In order to preserve spatial information without increasing the noise due to intersubject spatial variations, (Ng et al., 2009) used 3D moment invariants to characterize the spatial distribution of fMRI activation maps. They were able to show that the spatial distribution of the activations varies between different tasks. In addition, they found that using 3D moment invariants to characterize the spatial variations of the activation statistics offered more sensitivity to changes in activation patterns than other commonly used methods.

2.5 3D Moment Invariants for PET Images

This thesis will explore the use of 3D moment invariants (3DMIs) to describe the spatial characteristics of PET images within a specific ROI. We will use the second order moments J_1 , J_2 and J_3 derived by (Sadjadi and Hall, 1980), as well as the third and fourth order moments B_3 and B_4 , respectively, derived by (Reiss, T. H., 1992). PET images of PD will be used to test the use of 3DMIs. PD is an ideal pathology to investigate the use of spatial information since the disease produces a very specific spatial pattern of radiotracer uptake that is different from that in healthy subjects. We will review the main characteristics of PD in the following chapter.

Chapter 3: Parkinson's Disease

3.1 Clinical Overview

Parkinson's disease (PD) is the second most common neurodegenerative disease and it is estimated that it affects nearly 100,000 Canadians (Parkinson Society Canada, 2003). The risk of developing the disease increases rapidly over the age of 60 years and less than 4% of all cases occur under the age of 50 years (Van Den Eeden et al., 2003). The lifetime risk has been estimated to be about 4% with men being almost twice as likely to develop PD as women (Dluzen and McDermott, 2000; Elbaz et al., 2002). Differences in the incidence of PD due to race and ethnicity have also been observed (Van Den Eeden et al., 2003). While most cases of PD are considered to be non-heritable (they are referred to as 'idiopathic' or 'sporadic' PD), it is now known that around 10% of cases arise due to genetic factors possibly related to protein degradation and mitochondrial function (Klein and Schlossmacher, 2006).

The classic picture of PD is that of a movement disorder, with the most common symptoms being tremor at rest, rigidity, difficulties initiating movements (called akinesia), slowness of movements (called bradykinesia) and postural instability (Jankovic, 2008). Interestingly, motor symptoms can be very asymmetric affecting one side of the body more than the other especially early on in the disease, a fact that is used for diagnostic purposes to differentiate PD from other neurodegenerative diseases (Gelb et al., 1999). It has lately become apparent that non-motor complications are also common in PD. For example, depression is now known to be a common co-morbid condition with estimates of its prevalence amongst PD patients ranging from ~10%-70% (Veazey, 2005). Other non-motor symptoms include anxiety, apathy, sleep disorders, gastrointestinal dysfunctions and more (Chaudhuri et al., 2006). The importance of these non-motor symptoms to the quality of life of PD patients is increasingly being recognized (Martinez-Martin, 2011).

The diagnosis of PD is done clinically and various rating scales are used to evaluate the amount of impairment and disability. The Hoehn & Yahr (H&Y) scale is commonly used to provide a general description of how PD symptoms progress and to provide a coarse comparison between different groups of patients (Hoehn and Yahr, 1967). The H&Y ratings range from 0 for no signs of disease to 5 for patients who need a wheelchair or are bedridden unless assisted. The most common scale for assessing detailed clinical disability and impairment is the Unified Parkinson's Disease Rating Scale (UPDRS; Movement Disorder Society, 2003). The UPDRS includes sections dedicated to the assessment of non-motor aspects of daily living (part I), motor aspects of daily living (part II), clinician-scored motor evaluation (part III) and treatment-related complications (part IV). The part III of the UPDRS is commonly used as a clinical measure of increasing motor disability as PD progresses, with scores ranging from 0 for complete absence of motor symptoms to a maximum score of 108 for severe, bilateral symptoms.

The pathology of PD is associated with the degeneration of neurons that innervate subcortical brain areas associated with motor, cognitive and limbic functions. These degenerating neurons originate in the substantia nigra pars compacta (SNc) of the midbrain and are associated with the production of the neurotransmitter dopamine (DA). The reduced levels of DA are then thought to disrupt brain circuits responsible for the control of motor functions. It is estimated that 50-80% of dopaminergic neurons are already lost by the time symptoms appear and the disease is diagnosed (Davie, 2008). PD is also characterized by the accumulation of the α -synuclein protein into aggregates called Lewy bodies (LB). Postmortem studies have shown that the distribution of LBs in the brain of PD subjects is generally correlated with the degree of clinical symptoms (Hurtig et al., 2000).

There is no method to prevent or delay the loss of dopaminergic neurons and currently there is no cure for PD. Existing treatments are therefore designed to alleviate symptoms by using medication, surgery, rehabilitation and other strategies as needed. Early during treatment, medication can provide effective symptom management for a wide range of patients. However, motor complications due to medication are commonly developed and an optimal tradeoff between good symptom management and undesirable side effects needs to be achieved (Royal College of Physicians and National Collaborating Centre for Chronic

Conditions, 2006). As the disease progresses and both symptoms and side effects worsen. In this case, medication is not an effective therapy and surgery becomes an option.

The main medications used to treat the motor symptoms of PD are levodopa, dopamine agonists and monoamine oxidase-B (MAO-B) inhibitors. Levodopa (LD) is the most widely used treatment for PD and is a dopamine precursor which is converted into dopamine by dopaminergic neurons. LD increases the amount of DA in the brain and temporarily reduces the motor symptoms of PD. LD is regularly used in combination with drugs which inhibit the synthesis and degradation of DA in order to prolong the action of LD. Unfortunately, the long term use of LD can lead to the development of undesirable motor complications, such as involuntary movements (called dyskinesias) and fluctuations in the response to the medication (Jankovic and Stacy, 2007).

Dopamine agonists and MAO-B inhibitors are used as complementary therapy to LD with the aim of improving symptom management and reducing motor complications. Dopamine agonists bind to dopamine receptors and activate them in the absence of dopamine. They have similar effects to LD and reduce the incidence of motor complications to LD (Tintner and Jankovic, 2003). However, dopamine agonists have side effects of their own, including psychiatric complications such as impulse control disorders (Bonuccelli and Ceravolo, 2008; Voon et al., 2011). MAO-B inhibitors increase the level of dopamine in the brain by blocking its metabolism. They are not as effective as LD or dopamine agonists in managing motor symptoms and are therefore used predominantly early in the disease for patients with mild symptoms (Jankovic and Poewe, 2012).

Surgery is commonly used for advanced patients when drug therapies are no longer sufficient to control symptoms and complications. Deep brain stimulation (DBS) is the most common surgical treatment and involves the implantation of a device which sends electrical impulses to specific areas of the brain. The areas commonly targeted for stimulation are the subthalamic nucleus (STN) and the globus pallidus (GP). The use of DBS can reduce symptoms and/or decrease medication side effects (Jankovic and Poewe, 2012). DBS is a major surgery and has associated risks, including the possibility of hemorrhage, infection and equipment malfunction (Doshi, 2011).

3.2 Neuroanatomy of Motor Function

As discussed above, PD is associated with the death of dopaminergic neurons in the SNc. The SNc is part of a group of nuclei in the brain collectively known as the *basal ganglia*. The basal ganglia are associated with various functions, including motor control, learning and action selection. As shown in Figure 3.1, the main components of the basal ganglia are the striatum (composed of the caudate and putamen), the globus pallidus (composed of the globus pallidus externa, GPe, and the globus pallidus interna, GPi), the substantia nigra (SN; composed of the SNc and the substantia nigra pars reticulata, SNr), and the subthalamic nucleus (STN). In addition to interconnections between different basal ganglia structures, they are also strongly connected to the cerebral cortex, thalamus and other brain areas.

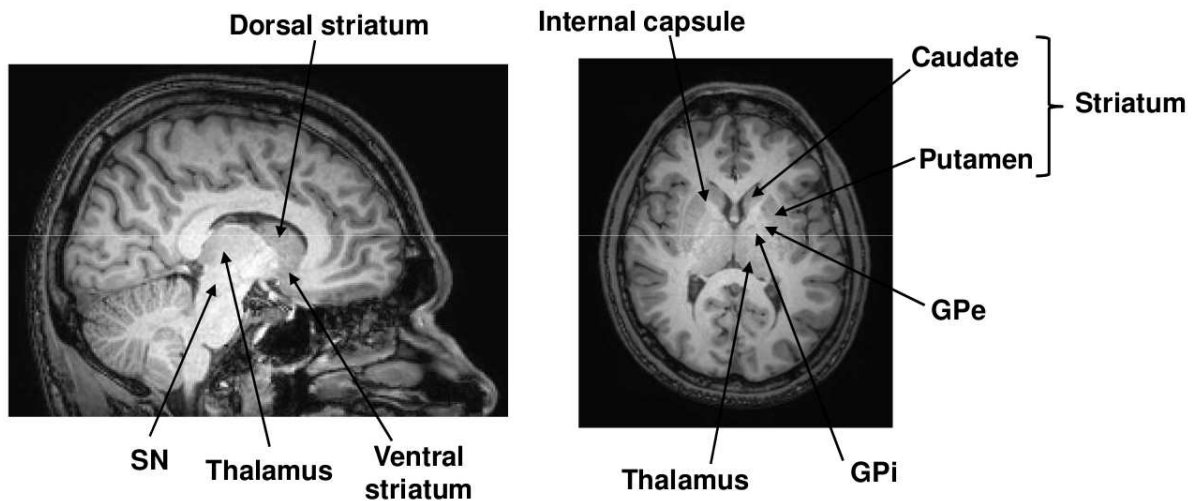


Figure 3.1: Anatomy of the basal ganglia in sagittal (left) and transverse planes (right).

The striatum is the largest nuclei in the basal ganglia and it has two distinct nuclei (the caudate and putamen) separated by a large tract of white matter (the internal capsule). The dopaminergic neurons in the SNc project to the striatum and supply regulatory DA input to these structures. The striatum also receives input from the cerebral cortex, with the caudate and putamen receiving input mostly from different parts of the cortex. In the globus pallidus,

both GPe and GPi receive input from the striatum with the GPe in turn projecting mainly to the STN while the GPi works together with the SNr projecting mainly to the thalamus.

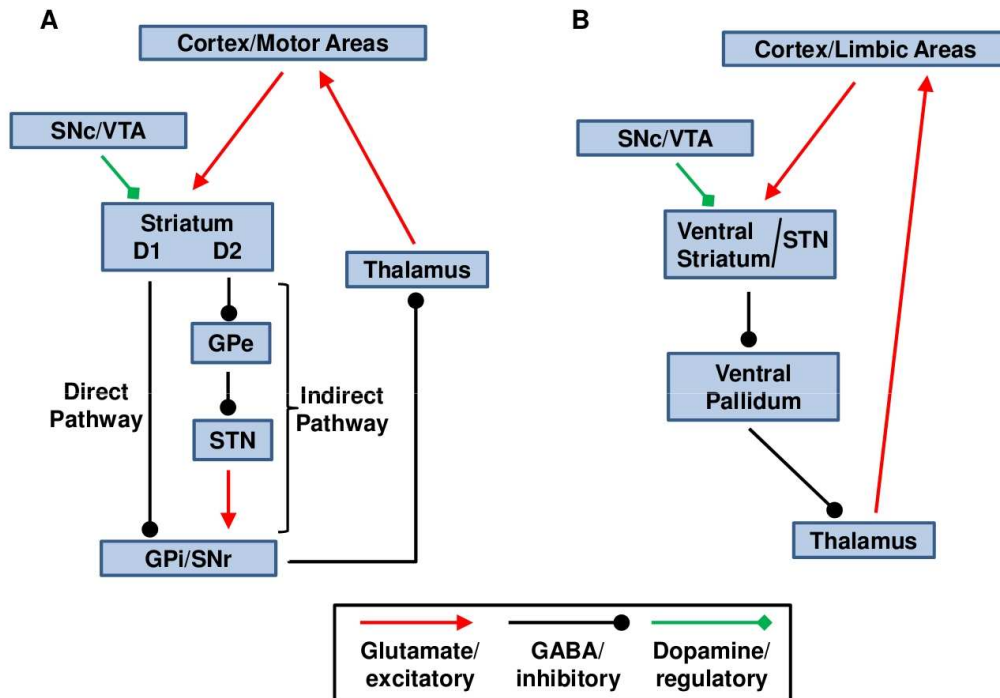


Figure 3.2: *The classical basal ganglia circuits involved in motor (A) and limbic (B) functions.*

The interconnections between the cerebral cortex, basal ganglia and thalamus allow them to work together to regulate motor, cognitive and limbic functions in the brain. The dorsal part of the striatum is largely involved in motor function, the intermediate parts in cognitive function, while the ventral part is involved in limbic function. For example, the classical model for understanding how the basal ganglia regulate motor and limbic functions is shown in Figure 3.2. The so-called motor circuit involves two pathways: a direct pathway and an indirect pathway (Figure 3.2, left). Here, the main input information arises from the cortex and enters the basal ganglia through the striatum. In turn, the main output structures are the GPi and SNr, which project out to the thalamus. The “direct” pathway involves direct connections between the striatum and the GPi/SNr through a monosynaptic γ -aminobutyric

acid (GABA, an inhibitory neurotransmitter) projection. The “indirect” pathway involves information relays at the GPe and STN through polysynaptic GABAergic and glutamatergic (excitatory) projections. Both pathways project to the cortex in the end, regulating instruction from the cortex to motor neurons in the body which either facilitate or inhibit movements.

In the direct pathway for motor function, the inhibition of the GPi/SNr by the striatum keeps structures in the thalamus and brainstem under reduced inhibition, allowing the thalamus to excite the cortex and allows movement to proceed. For the indirect pathway, inhibition of the GPe can reduce inhibition of the STN which in turn excites the GPi/SNr more. The GPi/SNr then inhibits the thalamus more, resulting in reduced stimulation of the cortex and suppression of movements. Here, the role of SNc (itself modulated by a nearby nucleus called the ventral tegmental area, VTA) is to modulate the entire circuit by supplying DA at the level of the striatum to excite the direct pathway (which contains D1 receptors, see Section 3.3) and inhibit the indirect pathway (which contains D2 receptors). Therefore, the injection of DA into the striatum promotes the execution of movements. This model helps us understand Parkinson's disease, where a *parkinsonian* state results from a reduced DA input from the SNc to the striatum, resulting in an overall inhibition of movements. On the other hand, a *dyskinetic* state results from the opposite case, where reduced activity of the STN results in an increase of involuntary movements.

In turn, the limbic circuit of the basal ganglia is thought to play a key role in the incentive, emotional and motivational aspects of motor movements. The neuroanatomy of this circuit is less well-understood and a general summary is shown in Figure 3.2 (right). For this circuit the limbic input arises from the frontal association cortex, cingulate gyrus, orbitofrontal cortex, amygdala and hippocampus (among others). In this case, the main input nucleus is the nucleus accumbens (also known as the ventral striatum, VS), which is made up of the ventromedial caudate, ventral putamen and olfactory tubercle. Parallel inputs into the STN are also present. The VS/STN then project to the ventral pallidum, which projects to the thalamus and then back to the cortex. This circuit is also regulated by the dopaminergic input from the SNc/VTA. This limbic circuit has been associated with the motivation required to learn motor tasks. Abnormal dopaminergic projections to this system from the SNc/VTA have been associated with addictive behaviors. In the case of addictions, the normal

modulation of behavioral responses to stimuli that activate feelings of reward (motivation) and the subsequent reinforcement these behaviors is believed to be disrupted.

The cortico-basal ganglia circuits described above have largely been thought of as segregated loops with limited sharing of information. However, recent findings have shown that the anatomical projections in these structures are much more complex than those shown in Figure 3.2. The largely expanded connections now known to exist between the different structures associated with the basal ganglia have motivated the revision of the classic models for their functionality shown in Figure Figure 3.2 (Draganski et al., 2008; DeLong and Wichmann, 2009; Marchand, 2010; Rommelfanger and Wichmann, 2010). These extended models have a larger degree of integration between the circuits. For example, (Marchand, 2010) suggests that the cortico-basal ganglia circuitry can represent a final common pathway from discrete brain regions to output signals encompassing motor, emotional and cognitive domains. As such, the varied information that is received by these structures can then be collected, funneled, integrated and processed by different circuits. While segregation can still be present, the degree by which the circuits are integrated and segregated can be determined with future studies. The fact that many diseases associated with these structures contain multiple motor, emotional, and cognitive aspects supports this view.

3.3 Dopamine System

At the molecular level, brain functions are modulated by neurotransmitters. Neurotransmitters are chemicals that transmit and modulate signals from neurons to their target cells across a junction called the *synaptic cleft*. Neurotransmitters are released from the neurons at the synaptic cleft and bind to *receptors* on the receiving cell. The binding of the neurotransmitter results in an activation of the cell in order to perform a specific function. Residual amounts of the neurotransmitter can be left at the synaptic cleft and must be cleared so that the synapse is ready to function again as soon as another neurotransmitter signal is

sent. The clearing is performed by either reabsorbing the neurotransmitter for future use by a *neurotransmitter transporter* or by breaking it down metabolically.

Neurotransmitters are produced in neurons from abundant and simple precursors commonly found in the body. They are then packaged and stored into *synaptic vesicles*. Vesicular transporters are proteins that move the neurotransmitters from the cytoplasm into the vesicles where they are then taken to the synaptic membrane and released into the synaptic cleft. Receptors on the opposite side of the synaptic cleft bind to the neurotransmitter. The receptors can either produce a postsynaptic potential which can be excitatory or inhibitory depending on the type of receptor and neurotransmitter. Receptors can also produce postsynaptic potentials that modulate (increase or decrease) excitatory or inhibitory signals.

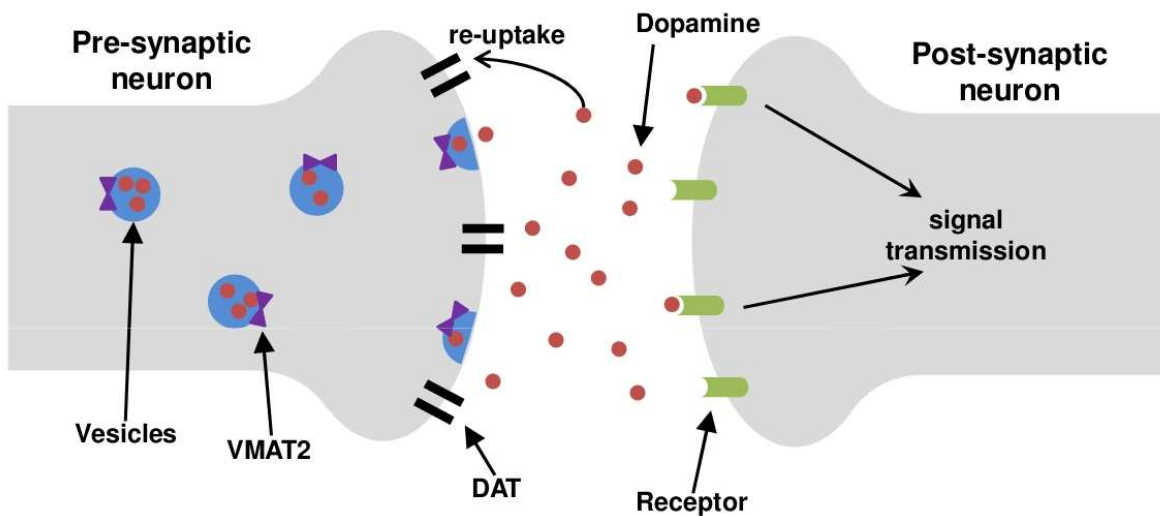


Figure 3.3: Schematic of a dopaminergic synapse showing pre-synaptic and post-synaptic components.

Dopaminergic neurons represent less than 1% of the total number of neurons in the brain (Chinta and Andersen, 2005). However, as described above, they play a very important part in modulating various brain functions such as motor behavior, motivation and working memory. Over 90% of dopaminergic neurons are located in the SNc and VTA, which as

described above project to various regions of the basal ganglia and cerebral cortex. These neurons produce dopamine and use vesicular monoamine transporters (VMAT) to store it into vesicles, in particular VMAT2 (Peter et al., 1995), as shown in Figure 3.3. After dopamine is released into the synapse it binds to receptors in the post-synaptic cell. Five subtypes of dopamine receptors mediate the action of dopamine: D1 and D5 belong to the D1-like family, while D2, D3 and D4 belong to the D2-like family (Missale et al., 1998; Beaulieu and Gainetdinov, 2011). The distribution of receptors varies in different tissues. For example, D1 and D2 are widely expressed in the striatum, while D3 has lower expression overall and is more commonly found in the ventral striatum and ventral parts of the GP. In order to recycle and clear dopamine from the synaptic cleft after it is released the dopamine transporter (DAT) is used.

3.4 PET Imaging of PD

A neurodegenerative disease like PD will reduce the number of neurons that produce dopamine, resulting in altered brain functions that depend on dopamine such as the ones described above. Neuroimaging of the dopamine system can then be used to study numerous pathological conditions in detail, including PD. Various PET radiotracers have been developed to study pre-synaptic and post-synaptic dopaminergic function. The pre-synaptic production and trapping of dopamine in vesicles can be studied with the dopamine precursor [^{18}F]Fluoro-L-dopa (FDOPA). The radiotracer [^{11}C]Dihydrotetrabenazine (DTBZ) or its ^{18}F -labeled analogue can be used to label VMAT2 and provide a measure of surviving dopaminergic terminals. Several molecules, including [^{11}C]Methylphenidate (MP), has been developed to label the DAT and provide an imaging measure of functioning dopaminergic terminals. Post-synaptically, radiotracers which compete with dopamine for receptor binding can be used to estimate changes in the amount of dopamine released into the synapse after an intervention. The D2/D3 receptor antagonist [^{11}C]Raclopride (RAC) can be used for this purpose. These, and other, PET radiotracers can then be used to study changes in the function of the dopamine system due to neurological diseases.

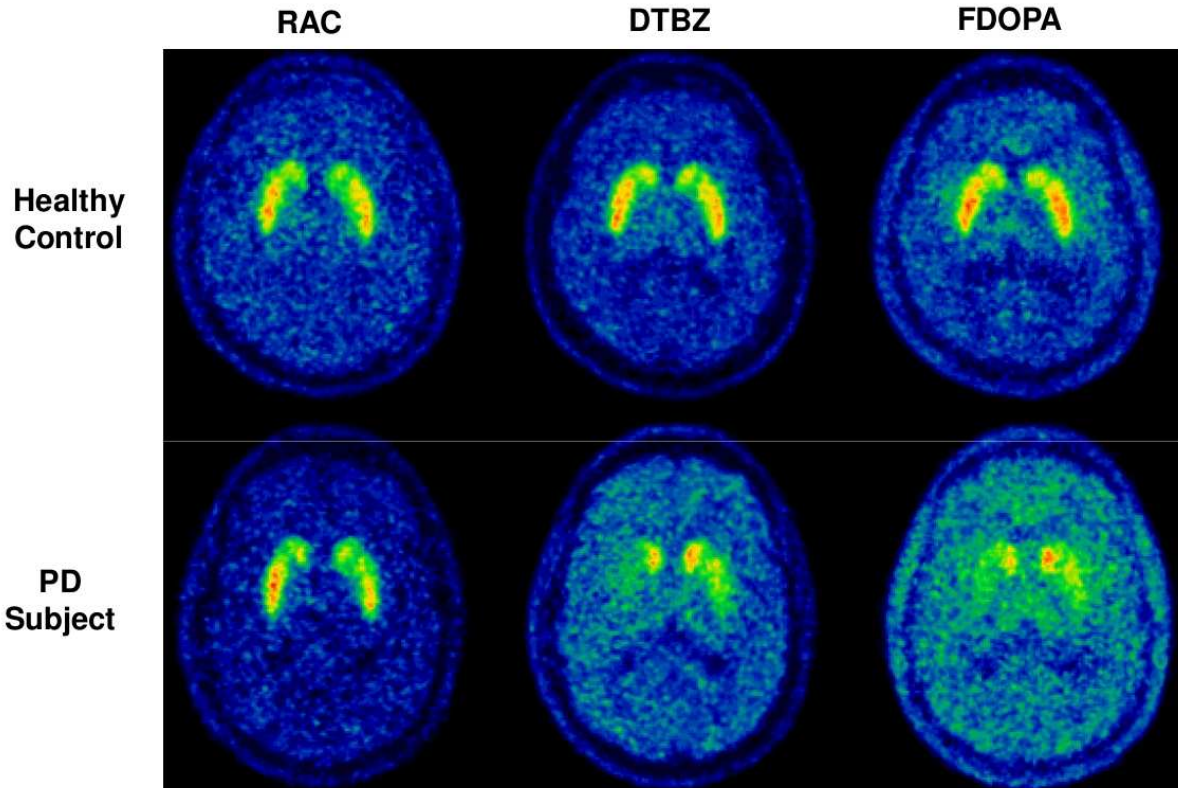


Figure 3.4: PET images using RAC (left), DTBZ (middle) and FDOPA (right) for a healthy control (top) and a subject with PD (bottom). The more affected side for this PD subject is the left side.

In PD, the above radiotracers have been used to assess disease progression, complications, effects of therapies and more (Stoessl et al., 2011). The kinetic modeling summarize in Section 1.6 can be used to derive binding potentials and uptake rate for the tracers of interest, which can then be used to understand how the disease operates at the molecular level. For example, DTBZ binding has been shown to decrease significantly as disease progresses, reflecting a reduced number of VMAT2 as dopaminergic neurons die. DTBZ binding has then been shown to provide a reliable imaging measure of disease progression (Lee et al., 2000; Nandhagopal et al., 2009). On the other hand, FDOPA uptake has been shown to be relatively preserved in the early disease, reflecting possible compensatory mechanisms, such as increased dopamine synthesis in the remaining dopaminergic neurons, to make up for the overall reduced production of dopamine (Lee et al., 2004; Hilker et al., 2005; Nandhagopal et al., 2009). RAC binding has been observed to be upregulated in early untreated PD and to be

relatively preserved as disease progresses (Rinne et al., 1995; Kaasinen et al., 2000). A sample set of PET images comparing a healthy control subject and a PD subject with these tracers is shown in Figure 3.4.

As RAC competes with dopamine for binding, a double RAC scan protocol (at baseline and after intervention) is used as a measure of intervention-induced changes in synaptic DA levels, often referred to as “intervention-induced dopamine release” by the pre-synaptic dopaminergic neurons. For example, if dopamine is released after the intervention, the RAC binding potential will be lower since receptors will be occupied by dopamine and the radiotracer will not be able to bind to them. The amount of dopamine released can then be estimated by calculating the change in the binding potential of RAC between a baseline scan (BP_{base}) and a scan done after the intervention (BP_{int}) as follows:

$$\text{Dopamine release (\%)} = \frac{BP_{base} - BP_{int}}{BP_{base}} \quad (3.1)$$

In PD, the amount of LD-induced dopamine release estimated using RAC has been shown to have a positive correlation to disease progression (Tedroff et al., 1996; de la Fuente-Fernández et al., 2001, 2004). This finding can be interpreted to mean that as disease progresses, the same amount of DA precursor (in this case LD) results in more dopamine being released faster into the synapse of the remaining neurons.

As we have seen, for DTBZ and FDOPA the kinetic properties of the tracer affected by PD are thought to reflect a decrease in storage capacity (related to increased death of dopaminergic neurons as the disease progresses) as well as functional changes in levodopa-derived dopamine kinetics. More importantly for this dissertation, we can see in Figure 3.4 that *the spatial distribution of the tracers also changes for PD subjects due to the disease*: the posterior parts of the putamen are significantly more affected than other anatomical regions in DTBZ and FDOPA images. This change reflects the spatial patterns of disease progression where the posterior parts of the striatum (in particular in the putamen, which is largely associated with motor function) are affected before the anterior parts. We can also see that another important aspect of the disease is reflected in the PET images: it is common for one side of the brain to be more affected than the other, especially early in the disease. This

results in an asymmetric tracer uptake between the two sides of the brain with one side appearing brighter.

Given the distinct change in spatial characteristics of PET images due to PD, the main goal of this dissertation is to derive an analysis method that will be able to quantify spatial changes and will be able to relate them to clinically-meaningful measures of disease progression. 3DMIs will be used to mathematically describe the spatial changes in PET images. Such analysis will be helpful when changes in the magnitude of a radiotracer binding/uptake remain the same when averaged within a specific anatomical region, but instead the spatial characteristics of the binding/uptake change. The next chapter will describe the use of 3DMIs for PET image of PD and the results obtained.

Chapter 4: 3D Moment Invariants for PET Images of Parkinson's Disease

4.1 Introduction

The goal of this dissertation is to explore whether 3DMIs derived from PET images of PD will help to characterize the spatial progression of PD-induced abnormalities of the dopaminergic system and relate them to clinical measures of disease progression. The particular research questions explored in this dissertation are:

- Are 3DMIs able to differentiate between healthy controls and PD patients?
- Do changes in 3DMIs have a strong relationship to clinically-meaningful PD severity and progression assessments? And,
- Can 3DMIs provide novel insights into levodopa-induced dopamine release as measured by a double RAC protocol?

Specifically, 3DMIs will be used to describe changes in the spatial characteristics of the dopaminergic function in PD in the following anatomical regions of the striatum: putamen, caudate and ventral striatum. As was described in Chapter 3, the putamen is involved in many motor functions and is significantly affected starting early in the disease. On the other hand, the caudate performs increasingly cognitive functions while the ventral striatum is largely involved in limbic functions. This study is particularly important for the last two regions (caudate and ventral striatum), where kinetic parameters generally do not show significant correlation with PD severity and where the effects of PD on cognitive and limbic functions can potentially be studied in more detail with this novel analysis method.

This chapter will first describe the analysis method that was developed to compute 3DMIs for PET images within an anatomically-derived ROI using MRI data. The results obtained for PD images will then be shown.

4.2 Materials

The data used for this project included five patients with PD and five healthy controls who were imaged with PET and MRI. All subjects underwent PET scans with three different radiotracers: RAC, DTBZ and FDOPA. For PD patients, anti-Parkinson medication was withdrawn 12 to 18 hours prior to scanning to minimize its effect on the data obtained. All PD patients underwent a double RAC protocol: a baseline scan and a scan on a different day beginning 1 hour following the open-label oral administration of levodopa/carbidopa (250/25mg, respectively). This double RAC protocol was used to estimate the amount of levodopa-induced dopamine release. In turn, DTBZ and FDOPA were used to study the amount of denervation and dopamine uptake rate, respectively.

4.2.1 PET Data

All PET scans were performed in 3D mode on the CTI/Siemens High Resolution Research Tomograph (HRRT). This dedicated brain PET camera has a field of view of 24 cm axially and 31.2 cm in-plane with an high intrinsic resolution of 2.5 mm (de Jong et al., 2007). A 10-minute transmission scan using an external ^{137}Cs source was performed before each emission scan for attenuation correction. Head motion was minimized using individually molded thermoplastic masks. Emission data were reconstructed using an ordinary Poisson ordered subset expectation maximization (OSEM-OP) algorithm with corrections for scatter, attenuation, randoms, and normalization (Polite and Snyder, 1991; Vandenberghe et al., 2001). Emission data were then corrected for motion by using the AIR software package. The final images had voxel size of $1.22 \times 1.22 \times 1.22 \text{cm}^3$.

For RAC and DTBZ scans, healthy controls were injected with 300 ± 25 MBq of activity and scanned for 1 hour. For RAC and DTBZ scans, PD patients were injected with 297 ± 20 MBq and 373 ± 3 MBq of activity, respectively, and scanned for 1 hour. Data from the DTBZ and RAC scan were framed into the following dynamic sequence: 4x1minute, 3x2minutes, 8x5minutes, 1x10minutes. For FDOPA scans, all subjects were injected with 257 ± 2 MBq of

activity and scanned for 1.5 hours (sequence: 18x5minutes). All subjects received oral administration of 200 mg of carbidopa 1 hour prior to FDOPA scanning to aid with radiotracer absorption.

4.2.2 MRI Data

All subjects also underwent an MRI scan to obtain anatomical information. An anatomical MRI image of all subjects was obtained using a 3T Philips Achieva scanner equipped with a head coil. T1-weighted images were taken using a turbo field echo (T1-TFE) sequence with TR=7.7ms, voxel dimensions of 1x1x1mm³, matrix size of 256x256 pixels, and 170 slices. Head motion was minimized by placing foam padding within the coil.

4.2.3 Subject Details

Of the five PD patients included in this study, four were receiving chronic levodopa treatment and three of these patients were also receiving direct DA agonists. One patient was receiving DA agonists alone. PD patients had mild to moderate PD, four had H&Y stage II, one had stage II.5. Group characteristics for PD and healthy controls are summarized in Table 4.1. For PD patients, motor performance testing was conducted off anti-Parkinson medication using the motor part of the UPDRS (part III). The study took place over an average of 37±29 days (except one healthy control where two of the four scans were taken two years apart). The study was approved by the University of British Columbia Clinical Ethics Board and all subjects gave written informed consent.

Table 4.1: Subject demographics*

Variable	HCs (n=5)	PDs (n=5)
Age, y	49(20)	63(6)
Male sex, No. (%)	2(40)	4(80)
PD duration, y	-	8.3(5.6)
H&Y stage, median (range)	-	2(2.0-2.5)
Levodopa usage, mg/d	-	475(217)
Dopamine agonist usage**, mg/d	-	193(135)
UPDRS motor score	-	18(11)

*Unless otherwise specified, values shown represent the mean and standard deviation.

**Dopamine agonist doses are given in levodopa equivalent units.

4.3 Methodology

4.3.1 Data Analysis

The T1-weighted MRI images were rebinned using trilinear interpolation to have a pixel size matching that of the PET images. For each subject, the PET images were then individually coregistered to the corresponding MRI image as follows: a total time-integrated emission image was derived from the dynamic PET data and coregistration was performed using the mutual information algorithm available in Statistical Parametric Mapping 8 (SPM8)³ software. A time-integrated emission image containing the last 30 minutes of the PET data was also calculated and the whole-brain rigid transformation matrix derived above was

³ Wellcome Trust Centre for Neuroimaging, UCL Institute of Neurology (<http://www.fil.ion.ucl.ac.uk/spm/software/spm8/>).

applied to it. The coregistered PET images were initially inspected by eye to look for any errors in the coregistration method. The coregistered 30 minute image was then used for subsequent analysis using 3DMIs as it is most representative of the spatial distribution of the tracer after it has reached equilibrium between plasma and tissue.

The T1-weighted MRI image of each subject was used to define anatomical ROIs corresponding to the left and right putamen, caudate and VS. The ROIs were drawn on each slice where the caudate and putamen were visible on the dorsal side of the striatum (where the effects of PD are most significant). The ROI definition of the VS was done following the method by Mawlawi et al. (2001). The ROIs were drawn by hand and were then exported to the corresponding baseline RAC image to carefully check for small coregistration errors and moved accordingly. Putamen and VS ROIs were never moved more than one pixel from the original MRI-based placement, while caudate ROIs (where partial volume effects are more important) were never moved more than two pixels from the MRI placement, within the spatial resolution of the PET images. These PET-optimized ROIs were then placed on all PET images for each subject to check that no residual coregistration errors remained. The values of the radiotracer concentration within the resulting ROIs were then extracted for all PET images of each subject. Sample images comparing the putamen concentrations of DTBZ between a healthy control and a PD patient are shown in Figure 4.1. These distributions containing the 3D coordinates of every voxel, (x, y, z) , as well as their radiotracer concentration value, $f(x, y, z)$, were then used to derive 3DMIs using Matlab as discussed below.

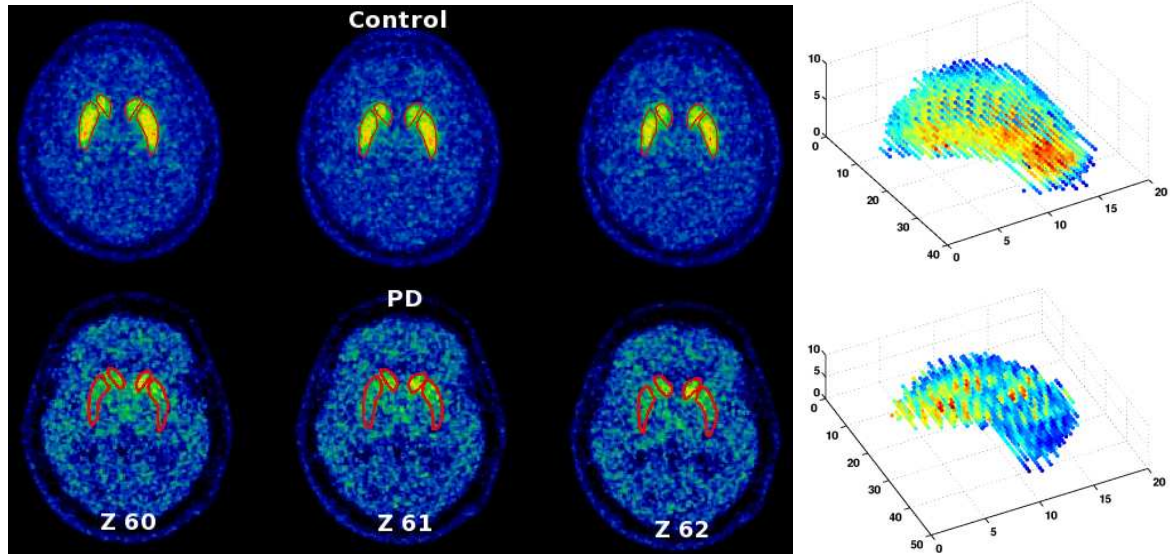


Figure 4.1: *Left - DTBZ images over three brain slices for a healthy control (top) and PD patient (bottom) with corresponding ROIs for the caudate and putamen. Right - Sample spatial distributions extracted for the right putamen for both subjects.*

To compare the results obtained from 3DMIs with traditional PET analysis methods we also calculated kinetic parameters for the radiotracers used here. In order to derive kinetic parameters for the same ROIs used to calculate 3DMIs, we produced parametric images of the radiotracer kinetics of interest. Here, kinetic parameters were derived for every voxel in the image using the original dynamic PET data as follows. For RAC and DTBZ we produced parametric images of their non-displaceable binding potentials (BP_{ND} , see Section 1.6) using a simplified reference tissue model as implemented in the Receptor Parametric Mapping software (Gunn et al., 1997). The cerebellum was used as the reference regions for RAC while the occipital cortex was used for DTBZ. For FDOPA, parametric images of the dopamine uptake rate constant (K_{occ} , see Section 1.6) were produced using the Patlak graphical method (Patlak and Blasberg, 1985) with the occipital cortex as the reference tissue. The resulting parametric images were then coregistered to the T1-weighted MRI images as described above. For all parametric images, the kinetic parameters for each ROI were calculated by averaging the voxel values contained within it.

Given that PD is a highly asymmetric disease and generally affects one side of the brain more than the other (especially early in the disease), this information was kept separate and the 3DMI and kinetic parameter values from both sides of the brain were not averaged.

4.3.2 3DMIs for PET Data

Five 3DMIs were calculated for each radiotracer image for ROIs that encompass the left and right caudate, putamen and VS. The 3DMIs are J_1 , J_2 , J_3 , B_3 and B_4 as defined in Equations 2.17 and 2.18. As was previously mentioned, J_1 represents the total spatial variance within the ROI, J_2 and J_3 incorporate spatial covariance as well as variance, while B_3 and B_4 include skewness and kurtosis, respectively, as well as other spatially descriptive terms.

Another important consideration when calculating 3DMIs is the distribution of voxel values, $f(x,y,z)$, in the image. There are no established guidelines for the optimum distribution of voxel values to use and this largely depends on the goals of the study. For example, some studies have chosen to re-map fMRI activation statistic values so that they lie between 0 and 1 for all subjects to minimize intersubject variability (Ng et al., 2009). In this case, the derived 3DMIs would be insensitive to overall magnitude changes in voxel values within the chosen ROI. Other studies have kept the original intensity values in the image (Morales et al., 2008), set all the voxel values to 1 (Mangin et al., 2004), and one study interested only in the shape of the surface of an ROI set all voxel values to 0 except at the surface of the area of interest where the values were set to 1 (Ward et al., 2007).

For the specific case of PET data of PD patients, magnitude changes in voxel values carry very useful information. For example, healthy controls have much higher radiotracer uptake due to intact dopaminergic terminals. When combined with the purely spatial changes within the ROI due to the disease, the resulting 3DMIs can be very powerful in discriminating between healthy controls and PD patients as well as characterizing differences in the same individual due to a pharmacological intervention (see results below). After testing various remapping schemes (including the ones described above), subtracting the minimum value within the ROI only and using the resulting voxel values to calculate the 3DMIs was found to

provide an appropriate balance between intersubject and intrasubject variability and useful magnitude changes in voxel values (see results below). The minimum value in the ROI was estimated by taking the median of the lowest 10 voxel values in the ROI and discarding voxels with values lower than the median. For example, this remapping scheme can account for differences such as those arising from changes in the specific amount of radiotracer activity injected between different subjects and between different scans of the same subject.

For all ROIs, the errors on the derived 3DMIs were estimated using the bootstrap method as implemented in the Matlab function ‘bootstp’ using 1,000 iterations for each ROI. The effect of the underlying background (e.g., due to non-specific binding) in the PET ROIs was studied and it does not significantly affect the 3DMIs: when the original voxel values are replaced by a random distribution with mean and standard deviation matching that of the background level the resulting 3DMIs are much smaller than those obtained with the original voxel values (by more than a factor of 10). Similarly, when adding this simulated background to the original voxel values the 3DMIs are <2% different from the original ones and within the estimated error bars, indicating that a uniform background would not affect significantly the calculated 3DMIs.

4.4 Results

This section describes the results obtained when 3DMIs were used to describe the spatial distribution of a radiotracer within an ROI in a PET image.

4.4.1 3DMIs Differentiate Between Healthy Controls and PD patients

3DMIs were found to successfully differentiate between healthy controls and PD patients, particularly for DTBZ (which is known to provide a reliable measure of neurodegeneration and thus disease severity). Figure 4.2 shows the measured spatial variance (J_I in Equation 5) for healthy controls and PD patients in the putamen, caudate and ventral striatum. For

comparison the values for DTBZ BP, FDOPA K_{occ} and RAC BP in those regions are also shown.

The spatial variance for DTBZ was significantly different for healthy controls and PDs in all ROIs studied here. In the putamen, where spatial asymmetries due to PD are largest, the moment B_3 (which has terms describing spatial asymmetries in the form of skewness, see Equation 2.18) also showed significant differences between healthy controls and PD patients for DTBZ images. The values for B_3 in the putamen are shown in Figure 4.3. Table 4.2 shows the statistical significances of a two-sample, two-tailed t-test between healthy controls and PD subjects calculated assuming they have unequal variances. As expected, DTBZ BP values were seen to decrease significantly for PD patients, especially in the putamen, reflecting a reduced number of pre-synaptic VMAT2 as dopaminergic neurons die. Differences between healthy controls and PD patients with FDOPA and RAC were not as widely seen as with DTBZ, a finding that is consistent with previous results involving FDOPA in compensatory mechanisms and RAC binding remaining relatively preserved as disease progresses.

It is then clear that 3DMIs, especially for DTBZ, can distinguish between healthy controls and PD patients with high significance in all ROIs studied here. In the case of RAC, the spatial variance (J_1) showed more significant difference between healthy controls and PD patients than BPs in the caudate and ventral striatum. While the differences were not as significant as those obtained using DTBZ BP and FDOPA K_{occ} , 3DMIs were found to have stronger correlations than kinetic parameters to estimates of denervation severity as measured using DTBZ and to clinical assessments of disease severity (see Sections 4.4.2 and 4.4.3).

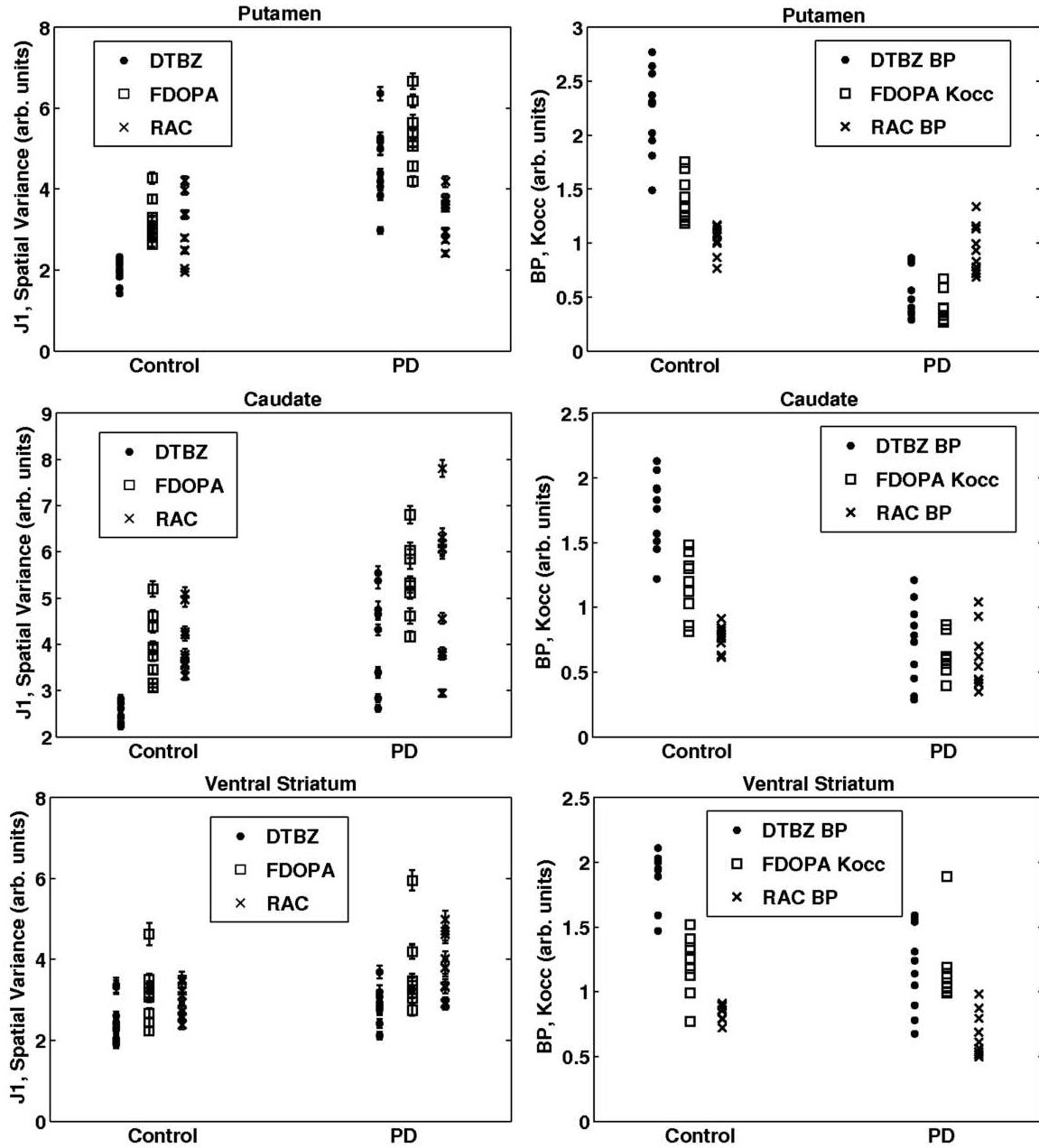


Figure 4.2: Left - Spatial variance (J_1) for healthy controls and PD subjects in the putamen, caudate and ventral striatum obtained from DTBZ (dot), FDOPA (square) and RAC (cross) images. Individual error bars in J_1 values were found by bootstrapping. Right - DTBZ BP, FDOPA Kocc and RAC BP values for the same ROIs.

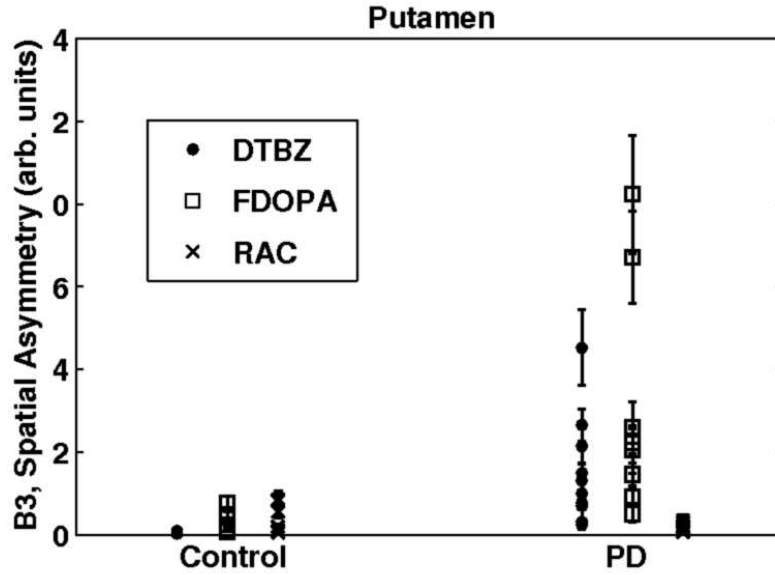


Figure 4.3: Spatial asymmetry (as measured using B_3) for healthy controls and PD subjects in the putamen for DTBZ (dots), FDOPA (square) and RAC (cross)

Table 4.2: Statistical differences (p - values) between healthy controls and PD subjects.

Tracer/Variable		Putamen	Caudate	Ventral Striatum
DTBZ	J_1	4×10^{-6}	9×10^{-4}	0.05
	B_3	6×10^{-3}	0.04	0.02
	BP	3×10^{-8}	7×10^{-7}	8×10^{-5}
FDOPA	J_1	2×10^{-5}	1×10^{-3}	0.13
	B_3	0.025	0.09	0.09
	K_{occ}	2×10^{-8}	2×10^{-4}	0.65
RAC	J_1	0.18	0.02	0.004
	B_3	0.38	0.08	0.03
	BP	0.23	0.04	0.006

The fact that relatively small 3DMI values with small variations were seen in healthy controls (see Figure 4.2 and Figure 4.3) reflects the fact that the shape of the anatomical structures *and* texture of the radiotracer concentrations within the members of this group are consistent. For PD patients, the larger value of 3DMIs with large variations between subjects can reflect the fact that there are more variations in the 3D shape *and/or* texture of the ROIs in this group. To differentiate between effects due to 3D shape versus texture, 3DMIs for each anatomical ROI were calculated where all voxel values have been manually set to a constant; in this case the value 1. Here, any variation in the resulting 3DMIs will be due to the 3D shape of the anatomical ROI only, and not its 3D texture. In this case, the 3DMIs of healthy controls and PD patients were indistinguishable: changes at the level of ~20% were seen across all subjects (see Figure 4.4). This suggests that the difference in 3DMIs between healthy controls and PD patients reflect mostly those differences to the 3DMIs provided by changes in the 3D texture, i.e., the spatial distribution of the radiotracer concentration within the ROI. This also illustrates the power of shape descriptors such as 3DMIs to characterize spatial distributions: they provide a wealth of information about both the 3D shape and texture within an ROI that can be applied to PET data.

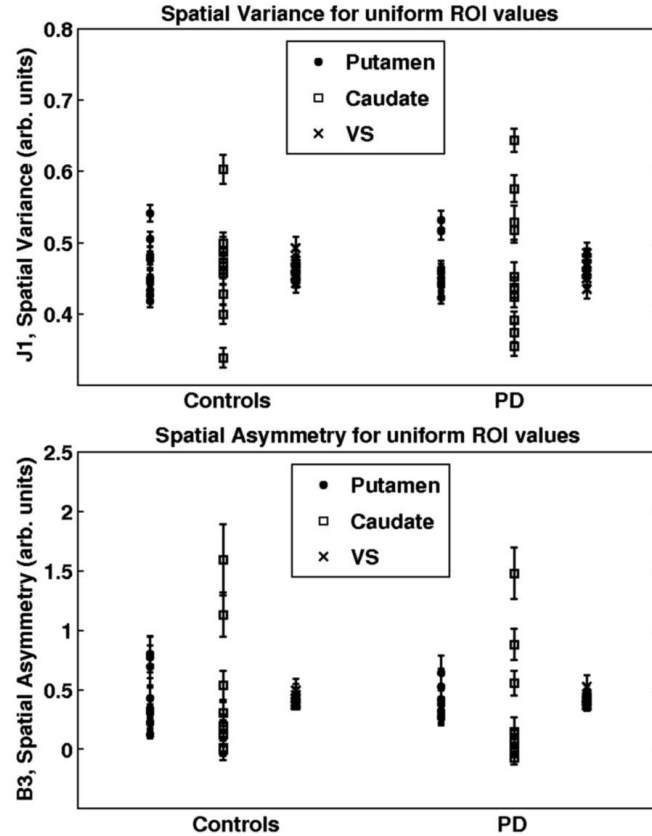


Figure 4.4: Spatial variance (J_1 , top) and asymmetry (B_3 , bottom) for all ROIs with voxel values replaced by 1.

4.4.2 3DMIs Correlate with PD Severity

Given that DTBZ is considered to be a reliable imaging marker of neurodegeneration, 3DMIs derived for this tracer are expected to be sensitive to changes due to advanced stages of neurodegeneration and therefore increased PD severity. 3DMIs were found to have a strong correlation with PD severity and to differentiate between the most and least affected sides of the brain. When comparing 3DMI values to clinical UPDRS scores for the left and right sides of each subject a strong positive relationship was found to be present⁴. The resulting plot for

⁴ Here, slightly modified UPDRS values were used so that the scores from motor deficits that are not side-specific (e.g., speech, posture, gait, etc) were added to the individual scores for the left and right sides of the

J_I is shown in Figure 4.5 (left column) for the putamen, caudate and VS. Values for DTBZ BP as a function of UPDRS are also shown in Figure 4.5 (right column).

In PD, the posterior parts of the striatum are affected first, giving patients with advanced disease a very one-sided or “skewed” spatial distribution that is most evident along the putamen with tracers such as DTBZ. Equation 2.18 shows that the expression for the B_3 moment invariant has terms that involve spatial skewness in each of the three spatial dimensions (e.g., μ_{300}). Therefore, in the putamen, B_3 values are also seen to be highly correlated to disease severity (see Figure 4.6).

As a first estimate, the data were tested for both a linear and exponential relationships between DTBZ 3DMIs and BPs as a function of UPDRS for PD patients (Nandhagopal et al., 2009). To test for an exponential relationship, the values were first linearized by taking the logarithm of both variables and then performing a linear regression. In most cases, an exponential relationship was found to be a better fit than a linear one with the current data (the only exception being B_3 in the putamen, which shows a more linear than exponential relationship). The best-fit regression results are shown in Table 4.3.

For DTBZ, 3DMIs were then found to have a stronger relationship to UPDRS than BPs in all ROIs studied here. This finding suggests that 3DMIs can be used independently of kinetic parameters to track the amount of degeneration present as disease progresses and its impact on motor performance.

body. These values were interpreted as representing UPDRS scores for each side that are more representative of the overall disease stage as well as maintaining information about the degree of disease asymmetry for each subject.

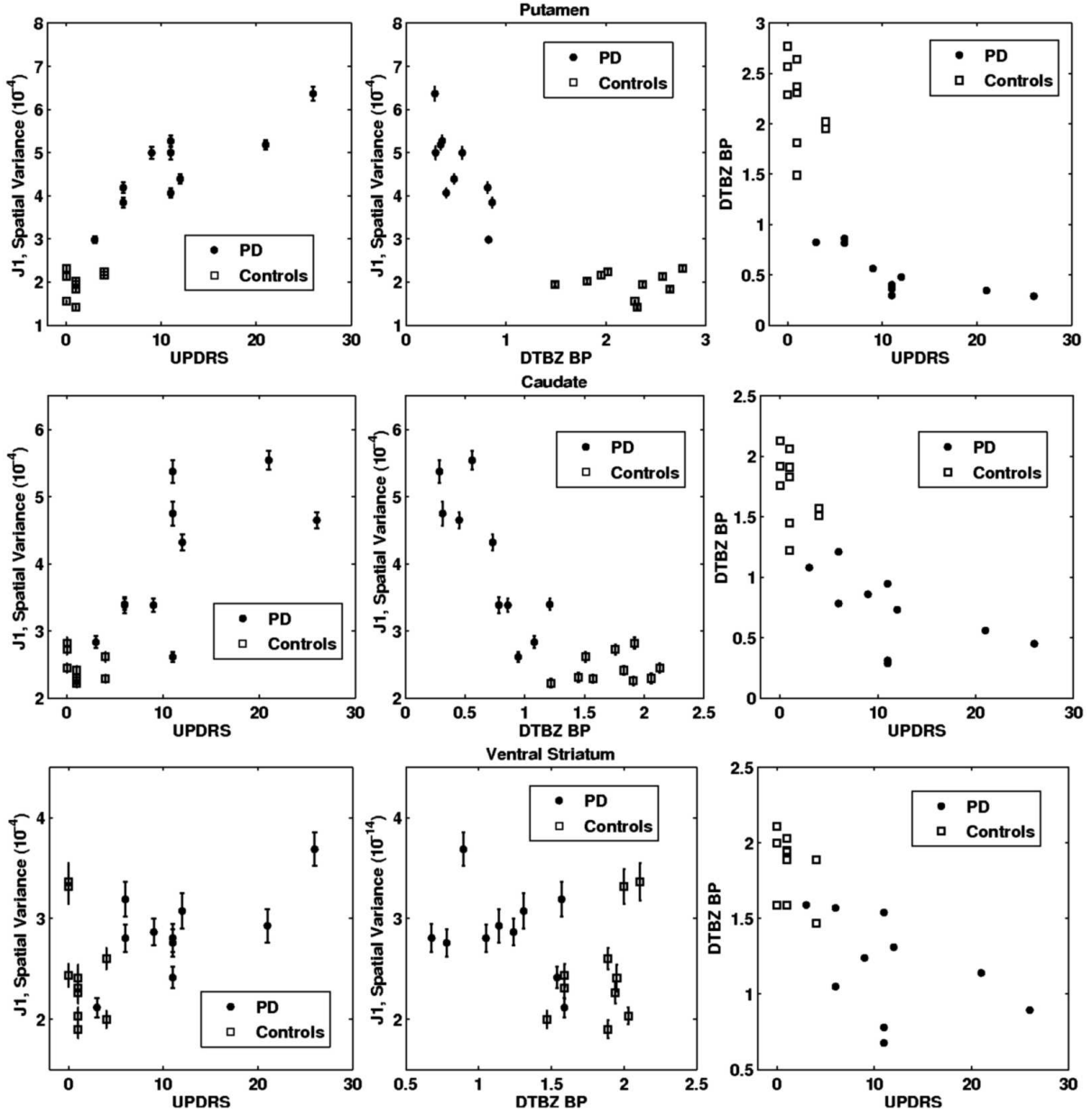


Figure 4.5: Spatial variance (J_1) in DTBZ images as a function of UPDRS (left) and DTBZ BP (middle) for the putamen (top), caudate (center) and ventral striatum (bottom). The corresponding values for DTBZ BP versus UPDRS are also shown (right). Each side of the brain is shown separately.

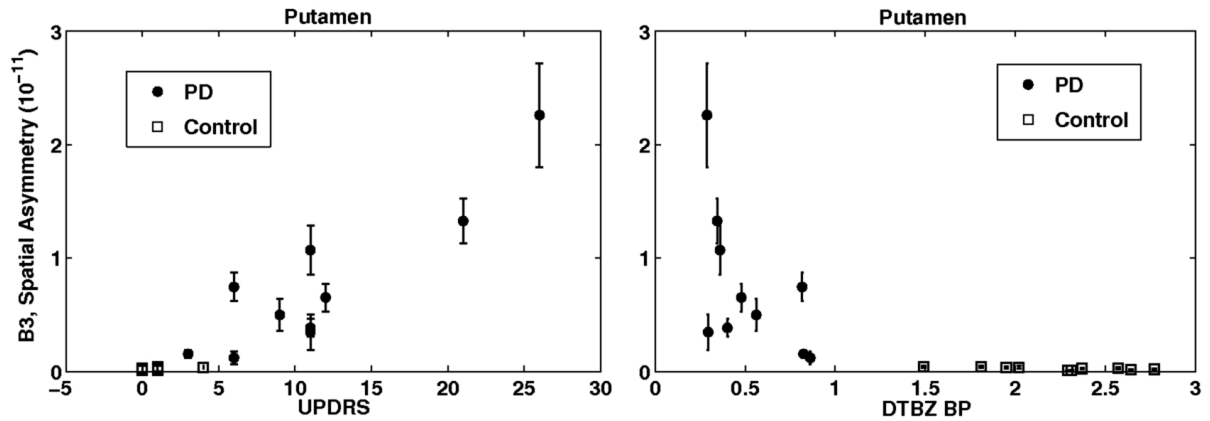


Figure 4.6: Spatial asymmetry (B_3) in DTBZ images of the putamen as a function of UPDRS (left) and DTBZ BP (right).

Table 4.3: Regression parameters for 3DMIs as a function of UPDRS for PD subjects. An exponential relationship was assumed and subsequently linearized.

Tracer/Variable		Putamen	Caudate	Ventral Striatum
DTBZ	J_1	$r=0.89, p=0.0005$	$r=0.68, p=0.03$	$r=0.67, p=0.03$
	B_3	$r=0.81, p=0.005^*$	$r=0.58, p=0.08$	$r=0.49, p=0.15$
	BP	$r=0.85, p=0.002$	$r=0.57, p=0.09$	$r=0.47, p=0.17$

*Regression using a linear relationship between B_3 and UPDRS provides a more significant correlation with $r=0.89$ and $p=0.0005$.

The above analysis was also carried out using the FDOPA images. In this case, no correlation of the resulting 3DMIs or K_{occ} with disease progression was found. This result is consistent with previous findings that show large variations in FDOPA uptake early in the disease, possibly associated with compensatory mechanisms (Lee et al., 2004; Hilker et al., 2005; Nandhagopal et al., 2009).

4.4.3 Levodopa-induced Spatial Changes Correlate with PD Severity

The changes in spatial characteristics of RAC images of PD patients after a dose of levodopa (LD) were also studied. The change in RAC BP after a single dose of LD is commonly used to estimate the amount of drug-induced synaptic dopamine (DA) release. One hypothesis of this dissertation is that the spatial characteristics of DA release will vary as PD progresses: early in the disease there will be a localized response to LD in the striatum (at the locations with large amounts of neurodegeneration), giving rise to a large change in the spatial characteristics and, in particular, a larger spatial variance after LD than before LD. In contrast, later in the disease a more uniform response might be expected throughout the largely affected striatum and, therefore, an unchanged or smaller spatial variance in the baseline RAC scan than after LD. On the other hand, it is known that the magnitude of the LD-induced changes in RAC BP increases for more severe disease, indicating a combination of decreased presynaptic buffering capacity and larger swing in synaptic DA levels before and after LD administration as the disease progresses.

Figure 4.7 (left) shows the RAC J_1 and BP values for healthy controls, PD patients before LD, as well as PD patients after LD in the putamen. A clear trend for increased J_1 values for PD patients after LD is visible. This increase makes PD values after LD different to those of controls at a statistically significant level ($p=0.02$). On the other hand, BP values in the putamen are not significantly different to controls before or after LD ($p=0.06$). The percent change in the 3DMI values before LD (e.g., $J_{1,before}$) and after LD (e.g., $J_{1,after}$) for each ROI was calculated as in the following example:

$$\Delta J_1 = \frac{J_{1,after} - J_{1,before}}{J_{1,before}} \quad (4.1)$$

The change in spatial characteristics before and after LD can then be correlated to relevant disease characteristics, such as severity and duration. Similar correlations in the estimated amount of DA release using the change in the derived RAC BPs as shown in Equation 3.1 can also be explored. A linear regression analysis shows that the change in spatial characteristics (here we concentrate on J_1 changes, ΔJ_1) are negatively correlated to the clinical assessment of disease severity (as measured using UPDRS) in the patients studied

here (see Figure 4.7, top centre). Conversely, ΔJ_1 was found to be positively correlated to DTBZ BP and thus increases as the number of surviving terminals increases (see Figure 4.7, top right). These relationships are very significant in the putamen with ($r=-0.78$, $p=0.0075$) for ΔJ_1 versus UPDRS and ($r=0.65$, $p=0.03$) for ΔJ_1 versus DTBZ BP.

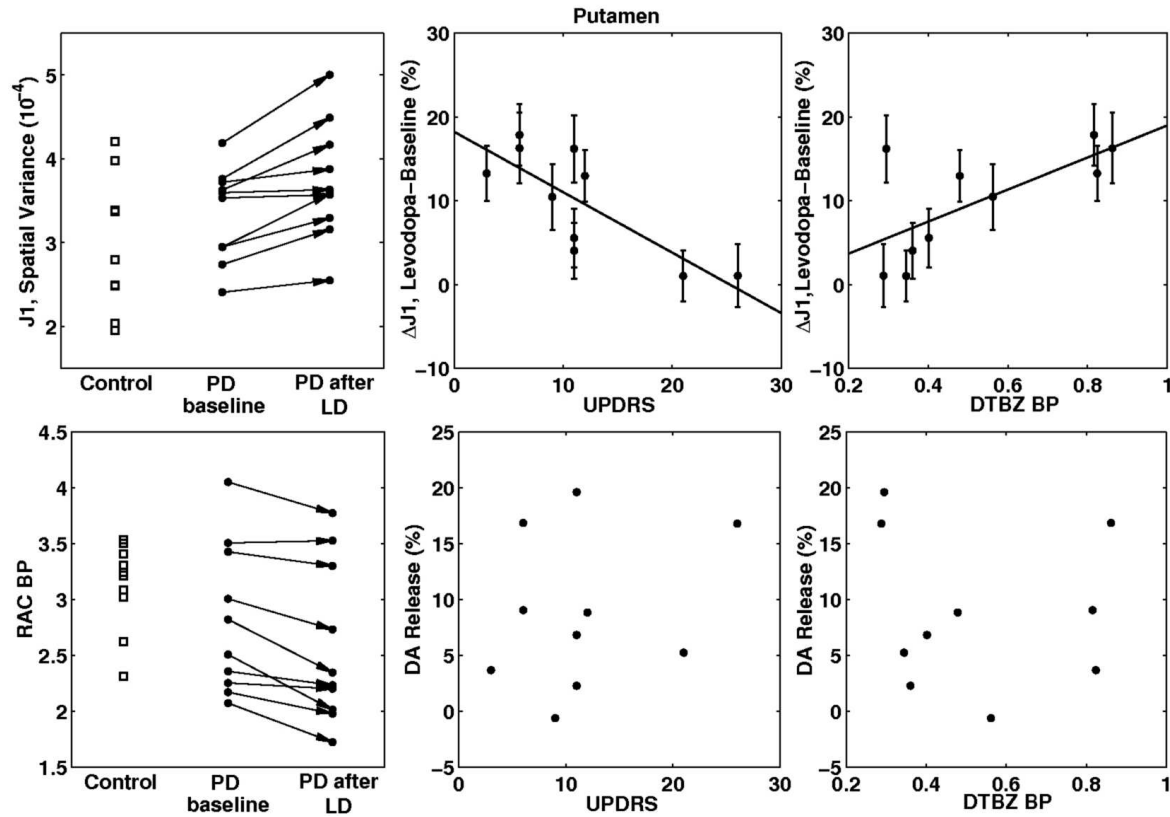


Figure 4.7: Levodopa-induced changes in the putamen. Left: RAC J_1 (top) and BP_{ND} (bottom) values for healthy controls, PD patients at baseline and PD after LD. Middle: Levodopa-induced changes in RAC J_1 (top) and DA release (bottom) as a function of UPDRS. Right: Levodopa-induced change in RAC J_1 (top) and DA release (bottom) as function of DTBZ BP.

On the other hand, DA release did not show any significant correlations with disease duration, age or severity for the subjects studied here⁵ (see Figure 4.7, bottom centre and

⁵ A marginal correlation of DA release with age was found in the putamen and caudate with $p=0.07$ in both regions.

right). While a correlation of DA release with disease duration has been shown to exist in the putamen (de la Fuente-Fernández et al., 2004), it is likely that the relatively low number of subjects did not allow this study to be sensitive to it. This fact, however, makes it more remarkable that strong correlations of ΔJ_I with UPDRS and DTBZ BP was seen and suggests that as disease progresses, not only is the amount of degeneration important for motor performance, but that the spatial characteristics of the degeneration is also key.

The decrease in ΔJ_I as disease progresses can be seen as a reflection of the widespread degeneration, which results in a more uniform spatial pattern of DA release, leading to unchanged or reduced spatial variance. Therefore, the spatial distribution of DA release before and after levodopa has great potential for providing additional information about how PD progresses and its effect on motor, cognitive and limbic functions, a finding that will be explored further in future work.

In the caudate and VS (see Figure 4.8 and Figure 4.9), both J_I and BP values were different to those of healthy controls at a statistically significant level ($p < 0.05$) both before and after LD. A significant negative correlation of ΔJ_I versus UPDRS was also present in the caudate ($r = -0.65$, $p = 0.03$). In the VS, this relationship was also significant after taking into account disease duration as a covariate ($r = -0.59$, $p = 0.03$). There was no significant correlation to disease duration by itself and its inclusion as a covariate did not change the correlation in the putamen or caudate. No significant correlation was found of ΔJ_I with age in any of the regions studied here and its inclusion as a covariate did not affect the results. As in the putamen, the estimated amount of DA released due to LD did not have a significant correlation to either UDPRS or DTBZ BP.

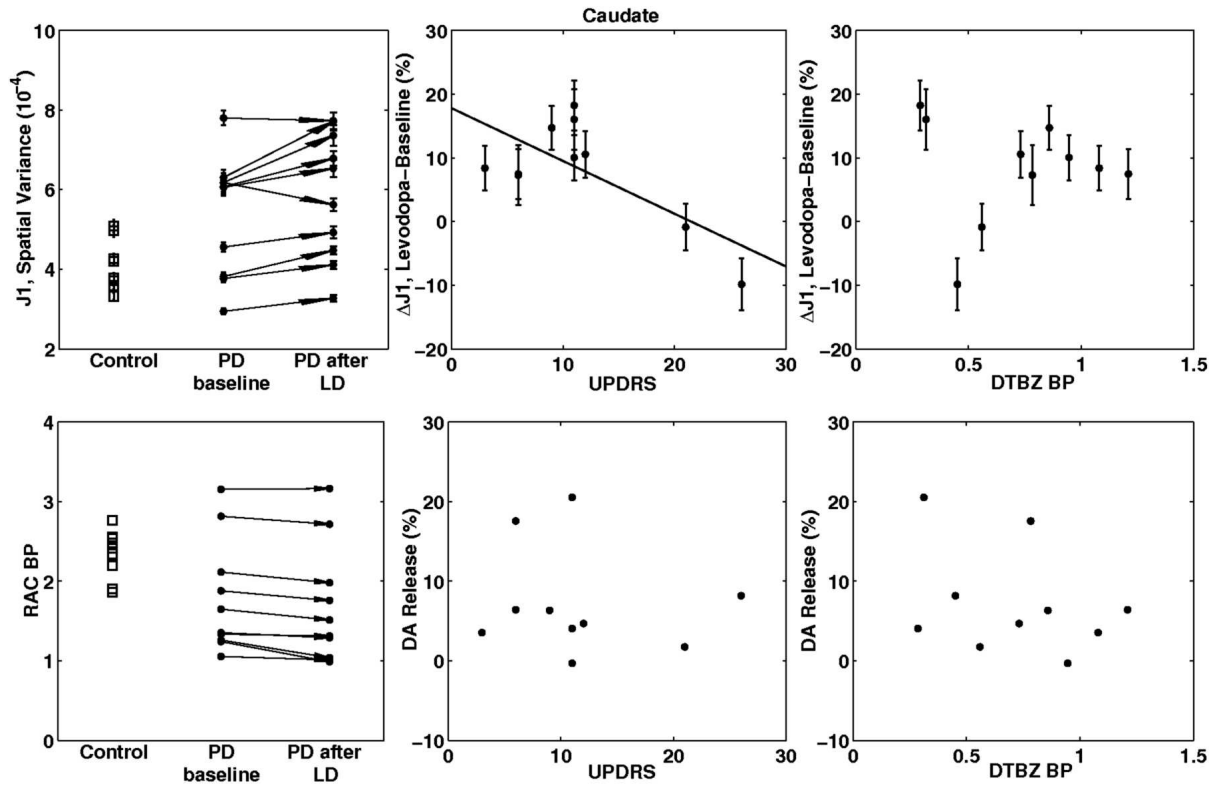


Figure 4.8: Same as Figure 4.7 but for the caudate.

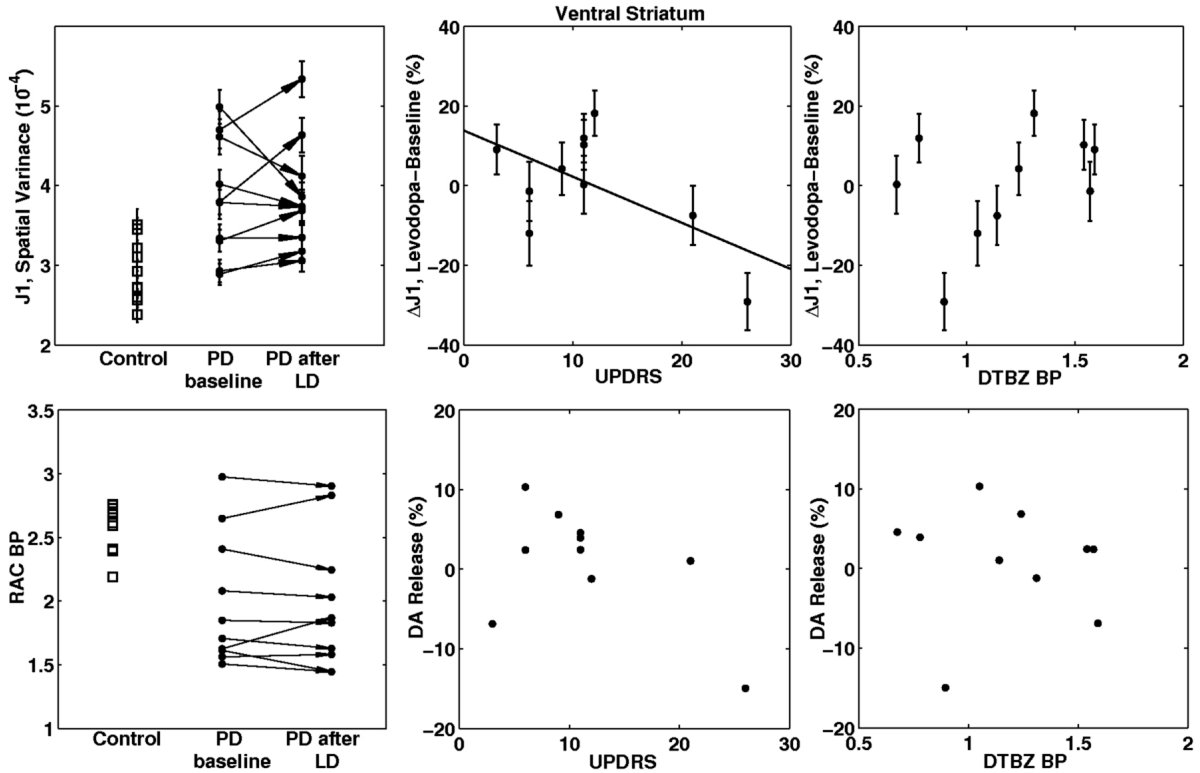


Figure 4.9: Same as Figure 4.7 but for the ventral striatum.

Unlike the putamen, ΔJ_1 did not have a statistically significant correlation to DTBZ BP in the caudate or ventral striatum. These areas are less affected by PD and this finding might not come as a surprise. However, from Figure 4.8 and Figure 4.9 it appears that the lack of correlation might be due to a couple of outliers. Specifically, there are two patients who (opposite to the above hypothesis) showed large ΔJ_1 values despite having low DTBZ BP and thus large amount of degeneration. One of these patients also showed a large ΔJ_1 and low DTBZ BP value in the putamen (see Figure 4.7 top right) and, interestingly, has reported strong motor side effects to treatment with LD and was switched to dopamine agonists to control PD symptoms. The other subject who only shows large ΔJ_1 values for low DTBZ BP in the caudate and ventral striatum has a history of possible psychiatric side effects to dopamine agonists in the form of impulse control disorders. While a study with larger number of patients is needed to establish any relationship between 3DMIs and potential side effects to treatment, these results are very encouraging.

Chapter 5: Discussion, Future Work and Conclusions

5.1 Discussion and Future Work

This dissertation shows that 3DMIs were able to provide a mathematical description of the spatial distribution of PET images within a ROI. 3DMIs were able to distinguish between healthy controls and PD subjects despite differences in the size and orientation of each subject's brain. In addition, changes in 3DMIs were found to have a strong relationship to clinically-assessed PD severity in all anatomical regions studied here.

Since 3DMIs can be thought of as measuring spatial deviations from smooth, symmetric distributions it should not be surprising that they are able to measure changes due to PD, which is well-known for having a very pathologically-specific spatial pattern. It is exciting and encouraging that 3DMIs show such strong relationship with clinical assessments of PD severity, opening a new window for studying this disease with PET images using spatial analysis. In particular, the term J_1 (a measure of spatial variance) was significantly correlated with disease severity in all the anatomical regions studied here, while the term B_3 (a measure of spatial asymmetry) was significantly correlated with disease severity in the putamen (where the PD-induced spatial asymmetry is particularly prominent).

The fact that a strong relationship with clinically-assessed PD severity was seen in both the caudate and the VS for J_1 (especially since FDOPA K_{occ} and DTBZ BP do not show such strong correlation) will be very important for the study of how PD affects these areas, which are associated with more cognitive and limbic functions than the putamen (Draganski et al., 2008; Marchand, 2010). This is particularly important since the significant effect of PD (and its associated treatment) on cognitive and limbic functions has recently been identified as a key aspect that affects the quality of life of PD patients and has therefore become a very active and significant area of research (Barone et al., 2009; Martinez-Martin, 2011).

Levodopa-induced changes in RAC J_1 values were negatively correlated to PD severity at a statistically significant level. This suggests that early in the disease a localized response to

the presence of exogenous DA (at locations with large amounts of degeneration) results in an increased value of spatial variance in the anatomical structures studied here. The fact that such a strong correlation was found with a small number of subjects suggests that the spatial distribution of the denervation can be an important tool to study the clinical progression of PD, especially in longitudinal studies where the magnitude of the tracer uptake might change relatively little but the spatial characteristics could provide a more sensitive progression biomarker.

The use of 3DMIs for PET imaging of other diseases is also very promising. For example, in oncology, quantifying tumor heterogeneity has recently been shown to be important for clinical outcomes (Eary et al., 2008; El Naqa et al., 2009) and 3DMIs might provide additional useful information in this area. Dopamine release studies in drug addiction and other neuropsychiatric disorders have sometimes produced puzzling results, such as the finding that there is no difference in the amount of DA released between oral versus intravenous doses of methylphenidate despite oral use rarely leading to addiction (Volkow et al., 2004; Shen et al., 2012). These, and many other research areas, might benefit from spatial analysis methods similar to the one presented here.

The use of 3DMIs for helping to translate research findings into clinical settings is also encouraging. A large stumbling block in this area has been the fact that the majority of neuroimaging research relates to comparisons across groups of subjects and conclusions about specific individuals is, in most cases, not feasible. For the study of neuroimaging spatial information, warping a subject's brains to a common template is not optimal toward the goal of developing clinical assessment tools that are relevant for individual subjects. However, 3DMIs allow us to retain an individual's spatial characteristics while being able to compare them to group values. The potential use for 3DMIs in a wide range of application is therefore large.

On the technical side, several questions remain open for the use of 3DMIs in neuroimaging research. Among them is the question of how high of a spatial resolution is needed to fully exploit the benefits of spatial analysis. The data for this dissertation used taken with one of the PET scanners with highest available spatial resolutions. To what extent a dataset with

lower resolution will impact the usefulness of spatial analysis remains to be explored, and the answer will most likely lie in the related question of: what is the relative size of the anatomical area of interest to the spatial resolution available for imaging? Further work on answering these questions in the context of PD can be explored in future efforts.

Additional research questions that remain to be explored include: how best to combine 3DMIs with traditional kinetic parameters (and any other relevance information, such as clinical and behavioral data) to better characterize diseases and assess their treatments? The use of machine learning algorithms and statistical classification schemes are increasingly being used in medical research (Shiraishi et al., 2011; Mwangi et al., 2012) and can be applied to this problem. In addition, the best way to perform segmentation for functional data has long been an important area of research with no clear answer (Zanotti-Fregonara et al., 2009; Dewalle-Vignion et al., 2012). This area of research is being explored in Dr. Sossi's group with the aim of combining anatomical and functional information to improve the segmentation results. On the other hand, it is also possible that the large-scale spatial changes in radiotracer uptake over the entire striatum can be enough on their own (without anatomical information) to provide the required spatial characteristics and this possibility can be explored in future work.

Finally, it is worth noting that 3DMIs are part of a wide range of spatial descriptors (Tesar et al., 2008; El Naqa et al., 2009; Flusser et al., 2009). While 3DMIs have been found to be very effective at describing the spatial changes observed in PET images of PD patients, there are many other spatial descriptors that may prove to be more useful for other imaging modalities and/or other diseases.

5.2 Conclusions

This dissertation explored the use of 3DMIs to characterize the spatial distribution of PET images within a ROI. This novel analysis method was applied to data from healthy controls and patients with PD. 3DMIs were able to successfully quantify the spatial differences between healthy controls and PD subjects and showed a strong correlation with PD severity

in all regions studied here (putamen, caudate and ventral striatum) for tracers that are known to track disease progression. In addition, 3DMIs were able to quantify levodopa-induced spatial changes in a double RAC protocol with the result that the largest increase in the spatial variance occurs early in the disease. This dissertation showed that the spatial characteristics of PET images can be used to assist in PD staging, diagnosis, assessing response and side-effects to therapies, and more. Spatial analysis of PET images such as the one carried out here may therefore have an important role to play in neuroimaging studies.

Bibliography

- Ashburner, J., Friston, K., 1997. Multimodal image coregistration and partitioning--a unified framework. *Neuroimage* 6, 209–217.
- Bailey, D.L., 2005. *Positron Emission Tomography*. Springer-Verlag London Limited, [New York].
- Barone, P., Antonini, A., Colosimo, C., Marconi, R., Morgante, L., Avarello, T.P., Bottacchi, E., Cannas, A., Ceravolo, G., Ceravolo, R., Cicarelli, G., Gaglio, R.M., Giglia, R.M., Iemolo, F., Manfredi, M., Meco, G., Nicoletti, A., Pederzoli, M., Petrone, A., Pisani, A., Pontieri, F.E., Quatrate, R., Ramat, S., Scala, R., Volpe, G., Zappulla, S., Bentivoglio, A.R., Stocchi, F., Trianni, G., Dotto, P.D., 2009. The PRIAMO study: A multicenter assessment of nonmotor symptoms and their impact on quality of life in Parkinson's disease. *Mov. Disord.* 24, 1641–1649.
- Beaulieu, J.-M., Gainetdinov, R.R., 2011. The physiology, signaling, and pharmacology of dopamine receptors. *Pharmacol. Rev.* 63, 182–217.
- Bloomfield, P.M., Spinks, T.J., Reed, J., Schnorr, L., Westrip, A.M., Livieratos, L., Fulton, R., Jones, T., 2003. The design and implementation of a motion correction scheme for neurological PET. *Phys Med Biol* 48, 959–978.
- Bonuccelli, U., Ceravolo, R., 2008. The safety of dopamine agonists in the treatment of Parkinson's disease. *Expert Opin Drug Saf* 7, 111–127.
- Brett, M., Johnsrude, I.S., Owen, A.M., 2002. The problem of functional localization in the human brain. *Nature Reviews Neuroscience* 3, 243–249.
- Chakeres, D.W., Schmalbrock, P., 1992. *Fundamentals of magnetic resonance imaging*. Williams & Wilkins, Baltimore.
- Chaudhuri, K.R., Healy, D.G., Schapira, A.H.V., 2006. Non-motor symptoms of Parkinson's disease: diagnosis and management. *Lancet Neurol* 5, 235–245.
- Chen, K., Chen, X., 2011. Positron emission tomography imaging of cancer biology: current status and future prospects. *Semin. Oncol.* 38, 70–86.
- Chinta, S.J., Andersen, J.K., 2005. Dopaminergic neurons. *The International Journal of Biochemistry & Cell Biology* 37, 942–946.
- Davie, C.A., 2008. A review of Parkinson's disease. *Br. Med. Bull.* 86, 109–127.
- de Jong, H.W.A.M., van Velden, F.H.P., Kloet, R.W., Buijs, F.L., Boellaard, R., Lammertsma, A.A., 2007. Performance evaluation of the ECAT HRRT: an LSO-LYSO double layer high resolution, high sensitivity scanner. *Phys Med Biol* 52, 1505–1526.
- de la Fuente-Fernández, R., Lu, J.Q., Sossi, V., Jivan, S., Schulzer, M., Holden, J.E., Lee, C.S., Ruth, T.J., Calne, D.B., Stoessl, A.J., 2001. Biochemical variations in the synaptic level of dopamine precede motor fluctuations in Parkinson's disease: PET evidence of increased dopamine turnover. *Ann. Neurol.* 49, 298–303.

- de la Fuente-Fernández, R., Sossi, V., Huang, Z., Furtado, S., Lu, J.-Q., Calne, D.B., Ruth, T.J., Stoessl, A.J., 2004. Levodopa-induced changes in synaptic dopamine levels increase with progression of Parkinson's disease: implications for dyskinesias. *Brain* 127, 2747–2754.
- DeLong, M., Wichmann, T., 2009. Update on models of basal ganglia function and dysfunction. *Parkinsonism Relat. Disord.* 15 Suppl 3, S237–240.
- Delso, G., Fürst, S., Jakoby, B., Ladebeck, R., Ganter, C., Nekolla, S.G., Schwaiger, M., Ziegler, S.I., 2011. Performance measurements of the Siemens mMR integrated whole-body PET/MR scanner. *J. Nucl. Med.* 52, 1914–1922.
- Dewalle-Vignion, A.-S., Yeni, N., Petyt, G., Verscheure, L., Huglo, D., Béron, A., Adib, S., Lion, G., Vermandel, M., 2012. Evaluation of PET volume segmentation methods: comparisons with expert manual delineations. *Nucl Med Commun* 33, 34–42.
- Dinelle, K., Ngo, H., Blinder, S., Vafai, N., Topping, G., Sossi, V., 2011. Frame-to-frame image realignment assessment tool for dynamic brain positron emission tomography. *Med Phys* 38, 773–781.
- Dluzen, D.E., McDermott, J.L., 2000. Gender differences in neurotoxicity of the nigrostriatal dopaminergic system: implications for Parkinson's disease. *J Gend Specif Med* 3, 36–42.
- Doshi, P.K., 2011. Long-term surgical and hardware-related complications of deep brain stimulation. *Stereotact Funct Neurosurg* 89, 89–95.
- Draganski, B., Kherif, F., Klöppel, S., Cook, P.A., Alexander, D.C., Parker, G.J.M., Deichmann, R., Ashburner, J., Frackowiak, R.S.J., 2008. Evidence for segregated and integrative connectivity patterns in the human Basal Ganglia. *J. Neurosci.* 28, 7143–7152.
- Eary, J.F., O'Sullivan, F., O'Sullivan, J., Conrad, E.U., 2008. Spatial Heterogeneity in Sarcoma 18F-FDG Uptake as a Predictor of Patient Outcome. *Journal of Nuclear Medicine* 49, 1973–1979.
- El Naqa, I., Grigsby, P.W., Apte, A., Kidd, E., Donnelly, E., Khullar, D., Chaudhari, S., Yang, D., Schmitt, M., Laforest, R., Thorstad, W.L., Deasy, J.O., 2009. Exploring feature-based approaches in PET images for predicting cancer treatment outcomes. *Pattern Recognition* 42, 1162–1171.
- Elbaz, A., Bower, J.H., Maraganore, D.M., McDonnell, S.K., Peterson, B.J., Ahlskog, J.E., Schaid, D.J., Rocca, W.A., 2002. Risk tables for parkinsonism and Parkinson's disease. *J Clin Epidemiol* 55, 25–31.
- Ercoli, L.M., W Small, G., Siddarth, P., Kepe, V., Huang, S.-C., Miller, K.J., Lavretsky, H., Bookheimer, S.Y., Barrio, J.R., Silverman, D.H.S., 2012. Assessment of dementia risk in aging adults using both FDG-PET and FDDNP-PET imaging. *International Journal of Geriatric Psychiatry*.
- Flusser, J., Suk, T., Zitov, B., 2009. Moments and moment invariants in pattern recognition. *J. Wiley, Chichester, West Sussex, U.K.; Hoboken, N.J.*
- Galvez, J.M., Canton, M., 1993. Normalization and shape recognition of three-dimensional objects by 3D moments. *Pattern Recognition* 26, 667–681.

- Gelb, D.J., Oliver, E., Gilman, S., 1999. Diagnostic criteria for Parkinson disease. *Arch. Neurol.* 56, 33–39.
- Gunn, R.N., Lammertsma, A.A., Hume, S.P., Cunningham, V.J., 1997. Parametric imaging of ligand-receptor binding in PET using a simplified reference region model. *Neuroimage* 6, 279–287.
- Guo, X., 1993. Three dimensional moment invariants under rigid transformation, in: Chetverikov, D., Kropatsch, W.G. (Eds.), *Computer Analysis of Images and Patterns*. Springer Berlin Heidelberg, Berlin, Heidelberg, pp. 518–522.
- Hilker, R., Schweitzer, K., Coburger, S., Ghaemi, M., Weisenbach, S., Jacobs, A.H., Rudolf, J., Herholz, K., Heiss, W.-D., 2005. Nonlinear progression of Parkinson disease as determined by serial positron emission tomographic imaging of striatal fluorodopa F 18 activity. *Arch. Neurol.* 62, 378–382.
- Hoehn, M.M., Yahr, M.D., 1967. Parkinsonism: onset, progression and mortality. *Neurology* 17, 427–442.
- Hofmann, M., Pichler, B., Schölkopf, B., Beyer, T., 2009. Towards quantitative PET/MRI: a review of MR-based attenuation correction techniques. *Eur. J. Nucl. Med. Mol. Imaging* 36 Suppl 1, S93–104.
- Hu, M.-K., 1962. Visual pattern recognition by moment invariants. *IEEE Trans Inf Theory* 8, 179–187.
- Hurtig, H.I., Trojanowski, J.Q., Galvin, J., Ewbank, D., Schmidt, M.L., Lee, V.M., Clark, C.M., Glosser, G., Stern, M.B., Gollomp, S.M., Arnold, S.E., 2000. Alpha-synuclein cortical Lewy bodies correlate with dementia in Parkinson's disease. *Neurology* 54, 1916–1921.
- Ishii, K., Willoch, F., Minoshima, S., Drzezga, A., Ficarò, E.P., Cross, D.J., Kuhl, D.E., Schwaiger, M., 2001. Statistical brain mapping of 18F-FDG PET in Alzheimer's disease: validation of anatomic standardization for atrophied brains. *J. Nucl. Med.* 42, 548–557.
- Jankovic, J., 2008. Parkinson's disease: clinical features and diagnosis. *Journal of Neurology, Neurosurgery & Psychiatry* 79, 368–376.
- Jankovic, J., Poewe, W., 2012. Therapies in Parkinson's disease. *Current opinion in neurology*.
- Jankovic, J., Stacy, M., 2007. Medical management of levodopa-associated motor complications in patients with Parkinson's disease. *CNS Drugs* 21, 677–692.
- Jin, L., Tianxu, Z., 2004. Fast algorithm for generation of moment invariants. *Pattern Recognition* 37, 1745–1756.
- Kaasinen, V., Ruottinen, H.M., Någren, K., Lehtikoinen, P., Oikonen, V., Rinne, J.O., 2000. Upregulation of putaminal dopamine D2 receptors in early Parkinson's disease: a comparative PET study with [11C] raclopride and [11C]N-methylspiperone. *J. Nucl. Med.* 41, 65–70.
- Klein, C., Schlossmacher, M.G., 2006. The genetics of Parkinson disease: implications for neurological care. *Nature Clinical Practice Neurology* 2, 136–146.

- Lee, C.S., Samii, A., Sossi, V., Ruth, T.J., Schulzer, M., Holden, J.E., Wudel, J., Pal, P.K., de la Fuente-Fernandez, R., Calne, D.B., Stoessl, A.J., 2000. In vivo positron emission tomographic evidence for compensatory changes in presynaptic dopaminergic nerve terminals in Parkinson's disease. *Ann. Neurol.* 47, 493–503.
- Lee, C.S., Schulzer, M., de la Fuente-Fernández, R., Mak, E., Kuramoto, L., Sossi, V., Ruth, T.J., Calne, D.B., Stoessl, A.J., 2004. Lack of regional selectivity during the progression of Parkinson disease: implications for pathogenesis. *Arch. Neurol.* 61, 1920–1925.
- Li, Y., 1992. Reforming the theory of invariant moments for pattern recognition. *Pattern Recognition* 25, 723–730.
- Lo, C.-H., Don, H.-S., 1989. 3-D moment forms: their construction and application to object identification and positioning. *IEEE Trans Pattern Anal Mach Intell* 11, 1053–1064.
- Mangin, J.-F., Poupon, F., Duchesnay, E., Rivière, D., Cachia, A., Collins, D.L., Evans, A.C., Régis, J., 2004. Brain morphometry using 3D moment invariants. *Med Image Anal* 8, 187–196.
- Marchand, W.R., 2010. Cortico-basal ganglia circuitry: a review of key research and implications for functional connectivity studies of mood and anxiety disorders. *Brain Struct Funct* 215, 73–96.
- Martinez-Martin, P., 2011. The importance of non-motor disturbances to quality of life in Parkinson's disease. *J. Neurol. Sci.* 310, 12–16.
- Mawlawi, O., Martinez, D., Slifstein, M., Broft, A., Chatterjee, R., Hwang, D.R., Huang, Y., Simpson, N., Ngo, K., Van Heertum, R., Laruelle, M., 2001. Imaging human mesolimbic dopamine transmission with positron emission tomography: I. Accuracy and precision of D(2) receptor parameter measurements in ventral striatum. *J. Cereb. Blood Flow Metab.* 21, 1034–1057.
- Millán, R.D., Dempere-Marco, L., Pozo, J.M., Cebal, J.R., Frangi, A.F., 2007. Morphological characterization of intracranial aneurysms using 3-D moment invariants. *IEEE Trans Med Imaging* 26, 1270–1282.
- Missale, C., Nash, S.R., Robinson, S.W., Jaber, M., Caron, M.G., 1998. Dopamine receptors: from structure to function. *Physiol. Rev.* 78, 189–225.
- Mitsis, G.D., Iannetti, G.D., Smart, T.S., Tracey, I., Wise, R.G., 2008. Regions of interest analysis in pharmacological fMRI: how do the definition criteria influence the inferred result? *Neuroimage* 40, 121–132.
- Morales, D.A., Bengoetxea, E., Larrañaga, P., 2008. Selection of human embryos for transfer by Bayesian classifiers. *Computers in Biology and Medicine* 38, 1177–1186.
- Moses, W.W., Virador, P.R.G., Derenzo, S.E., Huesman, R.H., Budinger, T.F., 1997. Design of a high-resolution, high-sensitivity PET camera for human brains and small animals. *IEEE Transactions on Nuclear Science* 44, 1487–1491.
- Movement Disorder Society, 2003. The Unified Parkinson's Disease Rating Scale (UPDRS): status and recommendations. *Mov. Disord.* 18, 738–750.

- Mwangi, B., Ebmeier, K.P., Matthews, K., Douglas Steele, J., 2012. Multi-centre diagnostic classification of individual structural neuroimaging scans from patients with major depressive disorder. *Brain* 135, 1508–1521.
- Nandhagopal, R., Kuramoto, L., Schulzer, M., Mak, E., Cragg, J., Lee, C.S., McKenzie, J., McCormick, S., Samii, A., Troiano, A., Ruth, T.J., Sossi, V., de la Fuente-Fernandez, R., Calne, D.B., Stoessl, A.J., 2009. Longitudinal progression of sporadic Parkinson's disease: a multi-tracer positron emission tomography study. *Brain* 132, 2970–2979.
- Ng, B., Abugharbieh, R., Huang, X., McKeown, M.J., 2009. Spatial characterization of fMRI activation maps using invariant 3-D moment descriptors. *IEEE Trans Med Imaging* 28, 261–268.
- Ng, B., Palmer, S., Abugharbieh, R., McKeown, M.J., 2010. Focusing effects of L-dopa in Parkinson's disease. *Hum Brain Mapp* 31, 88–97.
- Nieto-Castanon, A., Ghosh, S.S., Tourville, J.A., Guenther, F.H., 2003. Region of interest based analysis of functional imaging data. *Neuroimage* 19, 1303–1316.
- Nutt, R., 2002. For: Is LSO the future of PET? *Eur. J. Nucl. Med. Mol. Imaging* 29, 1523–1525.
- Parkinson Society Canada, 2003. Parkinson's Disease: Social and Economic Impact.
- Patlak, C.S., Blasberg, R.G., 1985. Graphical evaluation of blood-to-brain transfer constants from multiple-time uptake data. Generalizations. *J. Cereb. Blood Flow Metab.* 5, 584–590.
- Peter, D., Liu, Y., Sternini, C., de Giorgio, R., Brecha, N., Edwards, R.H., 1995. Differential expression of two vesicular monoamine transporters. *J. Neurosci.* 15, 6179–6188.
- Politte, D.G., Snyder, D.L., 1991. Corrections for accidental coincidences and attenuation in maximum-likelihood image reconstruction for positron-emission tomography. *IEEE Trans Med Imaging* 10, 82–89.
- Reiss, T. H., 1992. Pattern recognition proceedings. vol. 3, Conference C : Image, speech, and signal analysis, in: International association for pattern recognition (Ed.), IEEE computer Society Press, Los Alamitos, CA; Brussels; Tokyo.
- Rinne, J.O., Laihin, A., Ruottinen, H., Ruotsalainen, U., Någren, K., Lehtikoinen, P., Oikonen, V., Rinne, U.K., 1995. Increased density of dopamine D2 receptors in the putamen, but not in the caudate nucleus in early Parkinson's disease: a PET study with [¹¹C]raclopride. *J. Neurol. Sci.* 132, 156–161.
- Rommelfanger, K.S., Wichmann, T., 2010. Extrastriatal dopaminergic circuits of the Basal Ganglia. *Front Neuroanat* 4, 139.
- Royal College of Physicians, National Collaborating Centre for Chronic Conditions, 2006. Parkinson's disease : national clinical guideline for diagnosis and management in primary and secondary care. Royal College of Physicians, London.
- Sadjadi, F.A., Hall, E.L., 1980. Three-dimensional moment invariants. *IEEE Trans Pattern Anal Mach Intell* 2, 127–136.

- Shen, L.-H., Liao, M.-H., Tseng, Y.-C., 2012. Recent Advances in Imaging of Dopaminergic Neurons for Evaluation of Neuropsychiatric Disorders. *Journal of Biomedicine and Biotechnology* 2012, 1–14.
- Shibuya, K., Yoshida, E., Nishikido, F., Suzuki, T., Tsuda, T., Inadama, N., Yamaya, T., Murayama, H., 2007. Limit of Spatial Resolution in FDG-PET due to Annihilation Photon Non-Collinearity, in: Magjarevic, R., Nagel, J.H. (Eds.), *World Congress on Medical Physics and Biomedical Engineering 2006*. Springer Berlin Heidelberg, Berlin, Heidelberg, pp. 1667–1671.
- Shiraishi, J., Li, Q., Appelbaum, D., Doi, K., 2011. Computer-aided diagnosis and artificial intelligence in clinical imaging. *Semin Nucl Med* 41, 449–462.
- Sossi, V., de Jong, H.W.A.M., Barker, W.C., Bloomfield, P., Burbar, Z., Camborde, M., Comtat, C., Eriksson, L.A., Houle, S., Keator, D., Knoss, C., Kraiss, R., Lammertsma, A.A., Rahmim, A., Sibomana, M., Teras, M., Thompson, C.J., Trebossen, R., Votaw, J., Walker, M., Wienhard, K., Wong, D.F., 2005. The Second Generation HRRT - a Multi Centre Scanner Performance Investigation. *IEEE*, pp. 2195–2199.
- Stoessl, A.J., Martin, W.W., McKeown, M.J., Sossi, V., 2011. Advances in imaging in Parkinson's disease. *Lancet Neurol* 10, 987–1001.
- Tedroff, J., Pedersen, M., Aquilonius, S.M., Hartvig, P., Jacobsson, G., Långström, B., 1996. Levodopa-induced changes in synaptic dopamine in patients with Parkinson's disease as measured by [¹¹C]raclopride displacement and PET. *Neurology* 46, 1430–1436.
- Tesar, L., Shimizu, A., Smutek, D., Kobatake, H., Nawano, S., 2008. Medical image analysis of 3D CT images based on extension of Haralick texture features. *Comput Med Imaging Graph* 32, 513–520.
- Tintner, R., Jankovic, J., 2003. Dopamine agonists in Parkinson's disease. *Expert Opin Investig Drugs* 12, 1803–1820.
- Tixier, F., Le Rest, C.C., Hatt, M., Albarghach, N., Pradier, O., Metges, J.-P., Corcos, L., Visvikis, D., 2011. Intratumor heterogeneity characterized by textural features on baseline 18F-FDG PET images predicts response to concomitant radiochemotherapy in esophageal cancer. *J. Nucl. Med.* 52, 369–378.
- Townsend, D.W., 2004. Physical principles and technology of clinical PET imaging. *Ann. Acad. Med. Singap.* 33, 133–145.
- Valencia, C., Villa-Uriol, M.C., Pozo, J.M., Frangi, A.F., 2010. Morphological descriptors as rupture indicators in middle cerebral artery aneurysms. *Conf Proc IEEE Eng Med Biol Soc* 2010, 6046–6049.
- Van Den Eeden, S.K., Tanner, C.M., Bernstein, A.L., Fross, R.D., Leimpeter, A., Bloch, D.A., Nelson, L.M., 2003. Incidence of Parkinson's Disease: Variation by Age, Gender, and Race/Ethnicity. *American Journal of Epidemiology* 157, 1015–1022.

- Vandenberghe, S., D'Asseler, Y., Van de Walle, R., Kauppinen, T., Koole, M., Bouwens, L., Van Laere, K., Lemahieu, I., Dierckx, R.A., 2001. Iterative reconstruction algorithms in nuclear medicine. *Comput Med Imaging Graph* 25, 105–111.
- Veazey, C., 2005. Prevalence and Treatment of Depression in Parkinson's Disease. *Journal of Neuropsychiatry* 17, 310–323.
- Volkow, N.D., Fowler, J.S., Wang, G.-J., 2004. The addicted human brain viewed in the light of imaging studies: brain circuits and treatment strategies. *Neuropharmacology* 47, 3–13.
- Voon, V., Sohr, M., Lang, A.E., Potenza, M.N., Siderowf, A.D., Whetteckey, J., Weintraub, D., Wunderlich, G.R., Stacy, M., 2011. Impulse control disorders in Parkinson disease: a multicenter case--control study. *Ann. Neurol.* 69, 986–996.
- Ward, A.D., Hamarneh, G., Ashry, R., Schweitzer, M.E., 2007. 3D shape analysis of the supraspinatus muscle: a clinical study of the relationship between shape and pathology. *Acad Radiol* 14, 1229–1241.
- Watson, C.C., Casey, M.E., Michel, C., Bendriem, B., 2004. Advances in scatter correction for 3D PET/CT. *IEEE*, pp. 3008–3012.
- Zanotti-Fregonara, P., Maroy, R., Comtat, C., Jan, S., Gaura, V., Bar-Hen, A., Ribeiro, M.-J., Trébossen, R., 2009. Comparison of 3 methods of automated internal carotid segmentation in human brain PET studies: application to the estimation of arterial input function. *J. Nucl. Med.* 50, 461–467.